Posted on 22 Nov 2022 — The copyright holder is the author/funder. All rights reserved. No reuse without permission. — https://doi.org/10.1002/essoar.10505286.1 — This a preprint and has not been peer reviewed. Data may be preliminary.

Performance of the Taiwan Earth System Model in Simulating Climate Variability Compared with Observations and CMIP6 Model Simulations

Yi-Chi Wang[1], Huang-Hsiung Hsu[1], Chao-An Chen[1], Wan-Ling Tseng[2], Pei-Chun Hsu[3], Yu-Luen Chen[2], Cheng-wei Lin[4], Li-Chiang Jiang[1], Yu-Chi Lee[1], Hsin-Chien Liang[2], and Lex Chang[1]

[1]Research Center for Environmental Changes, Academia Sinica
[2]Academia Sinica
[3]Research Center for Environmental Changes, Academia Sinica, Taipei, Taiwan
[4]Research Center for Environmental Changes

November 22, 2022

Abstract

This study evaluated the performance of the Taiwan Earth System Model version 1 (TaiESM1) in simulating the observed climate variability in the historical simulation of the Coupled Model Intercomparison phase 6 (CMIP6). TaiESM1 was developed on the basis of the Community Earth System Model version 1.2.2, with the inclusion of several new physical schemes and improvements in the atmosphere model. The new additions include an improved triggering function in the cumulus convection scheme, a revised distribution-based formula in the cloud fraction scheme, a new aerosol scheme, and a unique scheme for three-dimensional surface absorption of shortwave radiation that accounts for the influence of complex terrains. In contrast to the majority of model evaluation processes, which focus mainly on the climatological mean, this evaluation focuses on climate variability parameters, including the diurnal rainfall cycle, precipitation extremes, synoptic eddy activity, intraseasonal fluctuation, monsoon evolution, and interannual and multidecadal atmospheric and oceanic teleconnection patterns. A series of intercomparisons between the simulations of TaiESM1 and CMIP6 models and observations indicate that TaiESM1, a participating model in CMIP6, can realistically simulate the observed climate variability at various time scales and performs better than the other CMIP6 models in terms of many key climate features.

Performance of the Taiwan Earth System Model in Simulating Climate Variability Compared with Observations and CMIP6 Model Simulations

Yi-Chi Wang[1], Huang-Hsiung Hsu[1*], Chao-An Chen[1], Wan-Ling Tseng[1], Pei-Chun Hsu[1], Yu-Luen Chen[1], Chien-Wei Lin[1], Li-Chiang Jiang[1], Yu-Chi Lee[1], Hsin-Chien Liang[1], and Lex Chang[1]

[1]Research Center for Environmental Changes, Academia Sinica, Taipei, Taiwan

Corresponding author: Huang-Hsiung Hsu (hhhsu@gate.sinica.edu.tw)

Key Points:

- Climate variability in the historical simulation of Taiwan Earth System Model version 1 (TaiESM1) is evaluated.
- While still subject to several common biases of CMIP6 models, TaiESM1 is capable of realistically simulating most climate variability.
- TaiESM1 exhibits outstanding performance in many key climate features, including the diurnal rainfall phase, monsoon evolution, and teleconnection.

Abstract

This study evaluated the performance of the Taiwan Earth System Model version 1 (TaiESM1) in simulating the observed climate variability in the historical simulation of the Coupled Model Intercomparison phase 6 (CMIP6). TaiESM1 was developed on the basis of the Community Earth System Model version 1.2.2, with the inclusion of several new physical schemes and improvements in the atmosphere model. The new additions include an improved triggering function in the cumulus convection scheme, a revised distribution-based formula in the cloud fraction scheme, a new aerosol scheme, and a unique scheme for three-dimensional surface absorption of shortwave radiation that accounts for the influence of complex terrains. In contrast to the majority of model evaluation processes, which focus mainly on the climatological mean, this evaluation focuses on climate variability parameters, including the diurnal rainfall cycle, precipitation extremes, synoptic eddy activity, intraseasonal fluctuation, monsoon evolution, and interannual and multidecadal atmospheric and oceanic teleconnection patterns. A series of intercomparisons between the simulations of TaiESM1 and CMIP6 models and observations indicate that TaiESM1, a participating model in CMIP6, can realistically simulate the observed climate variability at various time scales and performs better than the other CMIP6 models in terms of many key climate features.

1 Introduction

The Taiwan Earth System Model version 1 (TaiESM1) was developed on the basis of the Community Earth System Model version 1.2.2 (CESM1.2.2; Hurrell et al., 2013) by implementing several improvements in the parameterization schemes in the atmospheric component of CESM1.2.2. The modifications include the following: 1) replacing the three-mode version of the Modal Aerosol Module (Liu et al., 2012) aerosol scheme with the Statistical-Numerical Aerosol Parameterization scheme (Chen et al., 2013); 2) replacing the trigger function in the Zhang–McFarlane convection scheme with one that considers convection inhibition and the initiation of elevated instability (Wang et al., 2015); 3) improvement in the cloud fraction scheme to allow cloud fraction determination based on the distribution of the total water content instead of the relative humidity threshold (Shiu et al., 2020); and 4) implementing a surface radiation scheme that considers the effect of three-dimensional topography on the absorption of shortwave solar radiation (Lee et al., 2013). Detailed descriptions of the developments and tuning of TaiESM1 and the evaluation of its performance based on the piControl run and historical runs conducted with the Coupled Model Intercomparison phase 5 (CMIP5) setup are provided in an accompanying report (Lee et al., 2020).

A basic requirement of a climate model is satisfactory performance in the simulation of mean climatology. In addition, a model used for future climate projections should be able to realistically simulate the observed climate variability at various time scales, which is modulated not only through the long-term mean climate state but also through feedback to the mean state. For this purpose, the TaiESM was designed to enhance the ability of simulating variability from diurnal to interdecadal time scales. The basic approach was to improve or implement parameterization schemes such that the modules could more realistically represent the observed temporal and spatial variations. In an accompanying report, Lee et al. (2020) demonstrated that the TaiESM, when driven by the forcing designed for the CMIP5 historical experiments, can simulate long-term climatological mean fields with a score higher than those of most other CMIP5 models. In this study, we further demonstrated the ability of TaiESM1 to simulate the seasonal cycle, monsoon evolution, synoptic and intraseasonal variability, characteristics of precipitation extremes, the diurnal cycle, the El Niño–Southern Oscillation (ENSO), interannual teleconnection variability, and oceanic interdecadal oscillations in the historical experiments of the Coupled Model Intercomparison Project phase 6 (CMIP6).

The remainder of the paper is organized as follows. The methodology for analyzing climate variability in various time scales is described in Section 2. An evaluation of the mean state and warming of the historical simulation is presented in Section 3. Section 4 presents the evaluation of seasonal evolution and major monsoon systems. Section 5 details intraseasonal and synoptic variability, extremes, and the diurnal rainfall cycle. Interannual–interdecadal variability is reported in Section 6, and conclusions are provided in Section 7.

2 Model, experimental setup, and data

The historical experiment was conducted using TaiESM1, driven by the forcing provided by the CMIP6 (Eyring et al., 2016) for the 1850–2014 period, following the procedure described by Lee et al. (2020). The historical run was initiated from the year 671 in the piControl run of TaiESM1 with a horizontal resolution of 0.9° latitude × 1.25° longitude and 30 vertical layers. The performance of the model was evaluated for two data periods: 1915–2014 and 1980–2014. The longer period was used in the evaluation of interdecadal variability, such as the Atlantic Multidecadal Oscillation (AMO) and the Pacific Decadal Oscillation (PDO), whereas the shorter period that covers the satellite observation era was used for evaluating phenomena of shorter time scales, such as seasonal, intraseasonal, synoptic, extreme weather, and interannual scales.

Table 1 presents all the CMIP6 historical model runs used in this study for evaluating the performance of TaiESM1. The data were downloaded from the CMIP6 archive (https://esgf-node.llnl.gov/search/cmip6/). However, selection of the models used in each analysis is based on the availability of the required variables for analysis. A complete list of the models used in the study can be found in Table S1. Table S2 lists the observational data sets used in this study for validation. Most of the free tropospheric variables were evaluated against the Collaborative Reanalysis Technical Environment Multi-Reanalysis Ensemble version 2 (MRE2; Potter et al., 2018). In addition, precipitation data obtained from the Global Precipitation Climatology Project (GPCP V2.3, 1980–2014; Adler et al., 2003; Huffman et al., 2009), outgoing longwave radiation (OLR, 1980–2014) from the Clouds and the Earth's Radiant Energy System (CERES; Smith et al., 2011; Wielicki et al., 1996), and sea-surface temperature (SST; HadSST V1.1, Rayner et al., 2003; 1980–2014 for the ENSO and 1915–2014 for the AMO and PDO) were used in the model evaluation. The historical warming trend was compared with two sets of observations: the Hadley Centre—Climate Research Unit Temperature Anomalies (HadCRUT; Jones et al., 2012) and the Berkeley Earth Surface Temperature (BEST; Rohde et al., 2013).

For evaluation of the climate mode, the empirical orthogonal function (EOF) method is commonly used to extract geographical patterns with maximum variability. However, using the EOF modes derived from models in model performance evaluation presents several challenges in comparison with the observed leading climate modes. For example, Lee et al. (2019) explored the interannual and decadal modes and found that the order of model-derived EOFs may need to be swapped before comparisons are made with the observed EOFs. This problem is more severe in the evaluation of climate modes, such as Pacific–Japan (PJ) and Pacific–North America (PNA) patterns, which do not explain variance as efficiently as other leading modes. To avoid the ordering of climate modes based on EOFs, Lee et al. (2019) proposed the common basis function (CBF) method, wherein model anomalies are projected onto the geographical patterns of the observed EOFs for comparison. We found that the derived model modes based on the CBF method are generally more consistent with the observed modes and that the CBF method provides a more consistent framework for model evaluation.

Model	Description	Spatial Resolution (# of lon × # of lat)
ACCESS-CM2	Commonwealth Scientific and Industrial Research Organisation (Australia)	192x144
ACCESS-ESM1-5		192x145
AWI-CM-1-1-MR	Alfred Wegener Institute, Helmholtz Centre for Polar and Marine Research (Germany)	384x192
AWI-ESM-1-1-LR		192x96
BCC-CSM2-MR	Beijing Climate Center, Beijing (China)	320x160
BCC-ESM1		128x64
CAMS-CSM1-0	Chinese Academy of Meteorological Sciences (China)	320x160
CanESM5	Canadian Centre for Climate Modelling and Analysis, Environment and Climate Change Canada (Canada)	128x64
CESM2-FV2	National Center for Atmospheric Research, Climate and Global Dynamics Laboratory (USA)	144x96
CESM2		288x192
CESM2-WACCM-FV2		144x96
CESM2-WACCM		288x192
CIESM	Department of Earth System Science, Tsinghua University (China)	288x192
CMCC-CM2-SR5	Fondazione Centro Euro-Mediterraneo sui Cambiamenti Climatici (Italy)	288x192
CNRM-CM6-1	Centre National de Recherches Météorologiques (France)	256x128
E3SM-1-0	Lawrence Livermore National Laboratory, Department of Energy (USA)	360x180
E3SM-1-1-ECA		360x180
E3SM-1-1		360x180
EC-Earth3	EC-Earth consortium, Rossby Center, Swedish Meteorological and Hydrological Institute/SMHI (Sweden)	512x256
EC-Earth3-Veg		512x256
EC-Earth3-Veg-LR		320x160
FGOALS-g3	Chinese Academy of Sciences (China)	180x80
FIO-ESM-2-0	First Institute of Oceanography, State Oceanic Administration (China)	288x192
GFDL-CM4	National Oceanic and Atmospheric Administration, Geophysical Fluid Dynamics Laboratory (USA)	288x180
GFDL-ESM4		288x180
GISS-E2-1-G	Goddard Institute for Space Studies, National Aeronautics and Space Administration (USA)	144x90
GISS-E2-1-H		144x90
HadGEM3-GCM1-LL	Met Office, Hadley Centre (UK)	192x144
INM-CM4-8	Institute for Numerical Mathematics, Russian Academy of Science, Moscow (Russia)	180x120
INM-CM5-0		180x120
IPSL-CM6A-LR	Institut Pierre Simon Laplace (France)	144x143
KACE-1-0-G	National Institute of Meteorological Sciences/Korea Meteorological Administration, Climate Research Division (Republic of Korea)	192x144
MCM-UA-1-0	Department of Geosciences, University of Arizona (USA)	96x80
MIROC6	Japan Agency for Marine-Earth Science and Technology (Japan)	256x128
MICROC-ES2L		128x64
MPI-ESM-1-2-HAM	ETH Zurich, Switzerland; Max Planck Institut fur Meteorologie (Germany)	192x96
MPI-ESM1-2-HR	Max Planck Institute for Meteorology (Germany)	384x192
MPI-ESM1-2-LR		192x96
MRI-ESM2-0	Meteorological Research Institute (Japan)	320x160
NESM3	Nanjing University of Information Science and Technology (China)	192x96
NorCPM1		144x96
NorESM2-LM		144x96

NorESM2-MM	Climate modeling consortium consisting of Center for International Climate and Environmental Research (Norway)	288x192
SAM0-UNICON	Seoul National University (Republic of Korea)	288x192
TaiESM1	Research Center for Environmental Changes, Academia Sinica (Taiwan)	288x192
UKESM1-0-LL	Met Office, Hadley Centre (UK)	192x144

Table 1: The 45 CMIP6 coupled atmosphere–ocean climate models used in the historical warming analysis.

3 Climatological state and the evolution of historical simulations

Figure 1 presents the model global mean of near-surface (2 m) air temperature (SAT) anomalies of the historical simulations of TaiESM1 with the mean temperatures in 1951–1980 as a reference. Two sets of observations, HadCRUT and BEST, were plotted for comparison. The gray lines in Figure 1 denote the temperature time series of other CMIP6 models. TaiESM1 responded with similar magnitudes of cooling to CMIP6 forcing during major volcanic eruptions, such as those of Krakatoa (1883), Agung (1963), and Pinatubo (1991), compared with observations, implying that the model sensitivity of radiative forcing to stratospheric aerosols is reasonable. From 1850 to 1950, the SAT anomaly in TaiESM1 was approximately 0.3℃ warmer than the observed anomaly; moreover, decadal fluctuations rather than a warming trend were noted before 1950. During this period, TaiESM1 was at the warmer end in the CMIP6 model spectrum of SAT anomalies. After 1960, the change in SAT simulated by TaiESM1 was close to the observed value in 2014. This feature is highly similar to the SAT evaluation when TaiESM1 was driven by CMIP5 historical forcing (Lee et al., 2020). The causes of the warm bias in the beginning of the period are unknown and require further investigation.

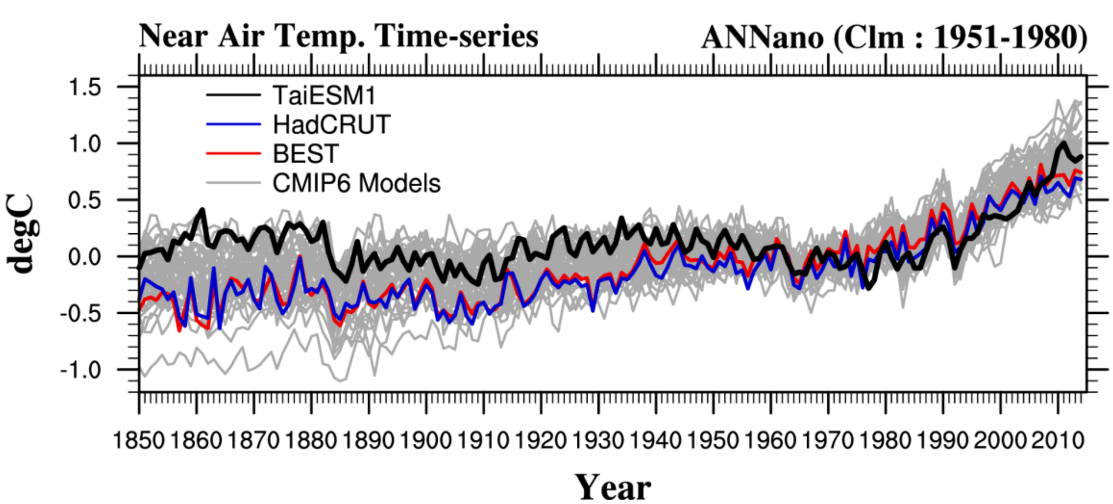

Figure 1: Historical warming trend of TaiESM1 with 1951–1980 as a reference (black line). Two sets of observed global temperature data, HadCRUT (blue) and BEST (red), are also shown for comparison. Temperature anomalies calculated from other CMIP6 models are presented as gray lines.

Figure 2 presents the global patterns of the observed annual mean precipitation and surface temperature and the corresponding values obtained using TaiESM1 (Figures 2a–f) and the performance of TaiESM1 compared with that of other CMIP6 models (Figure 2g). The multimodel ensemble (MME) means of rainfall and surface temperature denote the averages for all CMIP6 models listed in Table 1. The CMIP6 MME overestimated rainfall over the tropical oceans (Figure 2b), especially on the southern side of the equator, but underestimated rainfall over tropical lands such as the Amazon basin and Indian subcontinent, indicating the long-standing rainfall bias in previous CMIP simulations (Stephens et al., 2010). TaiESM1 demonstrated rainfall biases similar to those of other CMIP6 models in the overestimation of warm pool rainfall and the Intertropical Convergence Zone (ITCZ) over the eastern Indian and eastern Pacific oceans (Figure 2c). For near-surface temperature, TaiESM1 demonstrated a warm bias over the southern oceans and the west Eurasian continent but a colder bias in both the Arctic and Antarctica (Figures 2e and 2f).

The model performance rankings, shown in Figure 2g, were evaluated using the metrics introduced by Gleckler et al. (2008) through comparison of the relative performance with the median-performance model member among the CMIP6 models. The normalized space–time root-mean-square-error (RMSE) of selected variables, including air temperature, zonal and meridional wind velocity, and geopotential height at various pressure levels, and the SAT were evaluated against MRE2. Precipitation was evaluated against the GPCP, and radiation fluxes such as in total OLR, clear-sky upward longwave radiation, upward shortwave radiation in the total sky, and clear-sky shortwave radiation were evaluated on the basis of Clouds and Earth's Radiant Energy Systems Energy Balanced and Filled (CERES-EBAF; Loeb et al., 2018; Wielicki et al., 1996). The same evaluation was conducted for all CMIP6 models and the MME. Because the RMSEs of all models were compared with the median-performance model, high-performing models are shown in the lower part of the figure. Overall, TaiESM1 was among the top 50% of all of the CMIP6 models for performance in terms of the evaluated mean variables. Especially, it is in the top group for simulating tropospheric winds and temperature, except for the 200-hPa temperature, among the models.

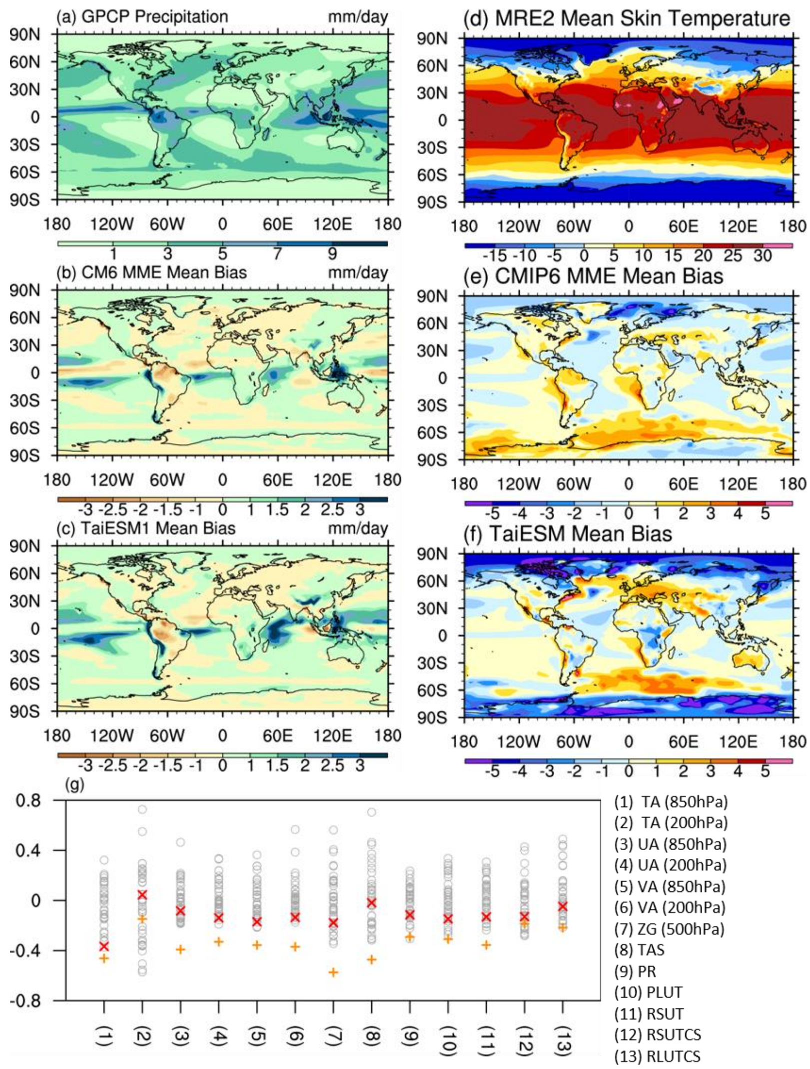

Figure 2: (a–f) Annual mean rainfall and surface temperature in observational analysis, and corresponding model biases of TaiESM1 and CMIP6 multiple model means with respect to observations. Observations used here are listed in Table 1. (g) Model ranking of basic mean variables compared with observations, following evaluation of the IPCC AR5 report. TaiESM1 is denoted by red crosses, and the CMIP6 multiple model mean is denoted by orange pluses. The air temperature is abbreviated as TA, zonal winds as UA, meridional winds as VA, geopotential height as ZG, longwave outgoing radiation as RLUT, shortwave upward radiation as RSUT, surface clear-sky shortwave upward radiation as RSUTCS, and surface clear-sky longwave upward radiation as RLUTCS.

4 Seasonal evolution and monsoons

4.1 Seasonal means

We evaluated the historical simulation (1976–2014) of tropical precipitation and circulation. The seasonal mean precipitation and circulation in the upper and lower troposphere during June–August (JJA) and December–February (DJF) are presented in Figure 3. TaiESM1 realistically simulated the major characteristics of seasonal mean fields. In the boreal summer (JJA, Figures

3a–c), major precipitation occurred over the ITCZ and the monsoonal regions of West Africa, South Asia, East Asia–Western North Pacific (EAWNP), and tropical America. As shown in Figure 3b, the monsoonal precipitation in South Asia and EAWNP, the associated planetary divergent flow, and regional monsoon circulation were well simulated. In the boreal winter (DJF, Figures 3d–f), major precipitation occurred in the Southern Hemisphere, which corresponds to the monsoons in Africa, the Maritime Continent, Australia, and South America. The upper tropospheric divergence center in winter was located over the Maritime Continent, whereas that in summer was located over South Asia and EAWNP.

Model biases in seasonal climatology could be quantitatively demonstrated through direct comparisons of model outputs with satellite observation and reanalysis data, as shown in Figures 3c and 3f. Differences at a confidence level of 99% are shown. TaiESM1 overestimated the summer precipitation over the equatorial Indian Ocean and central Pacific but underestimated the precipitation south of the Tibetan Plateau and the northern Bay of Bengal (Figure 3c). By contrast, the precipitation in extratropical East Asia was reasonably simulated. The biases are associated with excessively strong divergence in the central tropical and southeastern Pacific and a convergence bias in the tropical Atlantic and Western Africa. This planetary-scale divergence feature indicates the potential global impact of regional bias. As a result, a double ITCZ feature in the western/central tropical Pacific and the easterly was stronger than that observed in the tropical eastern Pacific. In winter (Figure 3f), the model overestimated the off-equatorial tropical precipitation with the double ITCZ feature in the eastern Pacific, whereas the precipitation in storm tracks was well simulated.

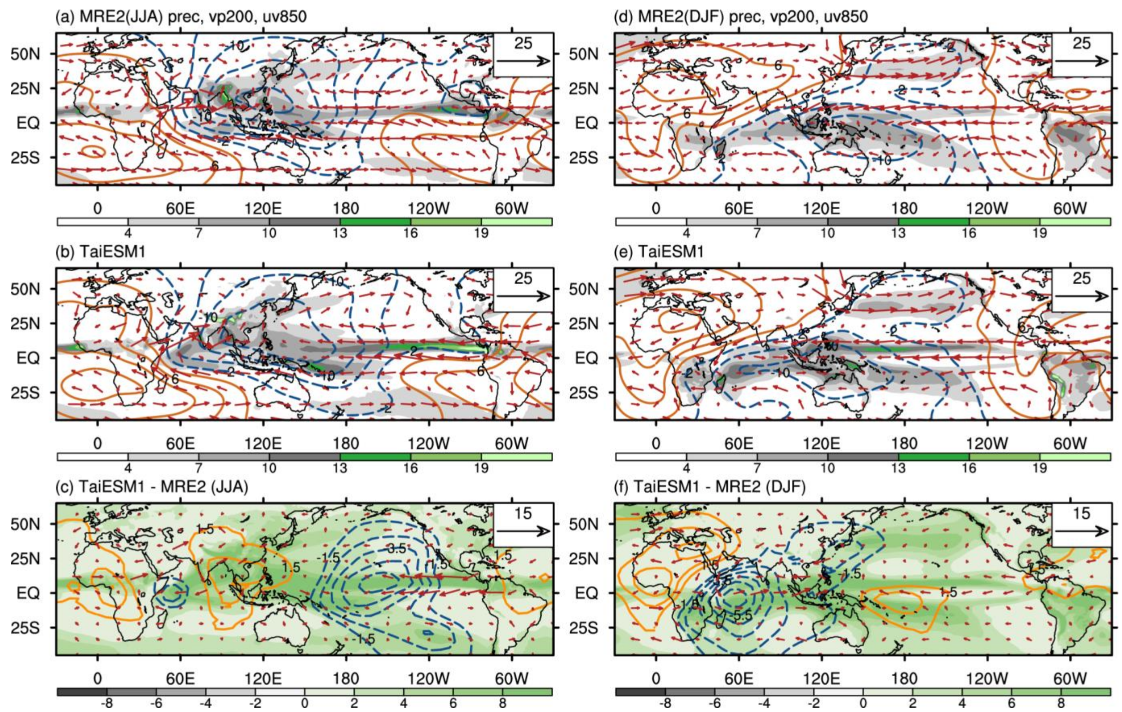

Figure 3. Precipitation (mm day^{-1}; shading), 200-hPa velocity potential (106 m^2 s^{-1}; contours), and 850-hPa wind (m s^{-1}; vectors) from the observation results (GPCP in 1997–2014; MRE2 in 1979–2005), TaiESM1 outputs (1979–2005), and TaiESM1 minus the observation results in (a–c) JJA and (d–f) DJF. Vectors in (a, b, d, and e) denote wind speeds higher than 3 m s^{-1}, and those in (c, f) denote a wind speed difference greater than 1 m s^{-1}. In (c, f), precipitation and velocity potential are shown when the differences between model outputs and observations have a confidence level of 99%.

TaiESM1 well presents the monsoonal winds in the lower troposphere (vectors in Figure 3). It successfully characterizes the southwesterly flow in West Africa, the Arabian Sea, and the South China Sea and the southeasterly flow in North America in summer, and the northeasterly flow in West Africa, the Arabian Sea, the South China Sea, and South America in winter. The surface temperature, OLR, and precipitation were also well represented by TaiESM1 (Figure 4). The ranking of the performance of the CMIP6 models based on the model–observation pattern correlations of surface temperature, OLR, and precipitation over North America, Africa, Asia, Australia, and the global domain is shown in Figure 4. In general, MME means have the optimal performance, while the individual models have more difficulty in representing JJA and DJF rainbands than representing the annual rainfall means (Figure 4a-c). Among the three variables, rainfall was the variable that the models exhibited the least ability to simulate, in all regions except for Africa. Notably, almost all models had difficulty simulating surface temperature in Africa and OLR in Australia during both JJA and DJF (Figure 4g-i and Figure 4j-l). The reasons underlying the biases in particular regions remain unclear and warrant further investigation. Overall, the ability of TaiESM1 to represent all three variables in all four regions was comparable to that of the MME of CMIP6 models, which achieved the highest rankings.

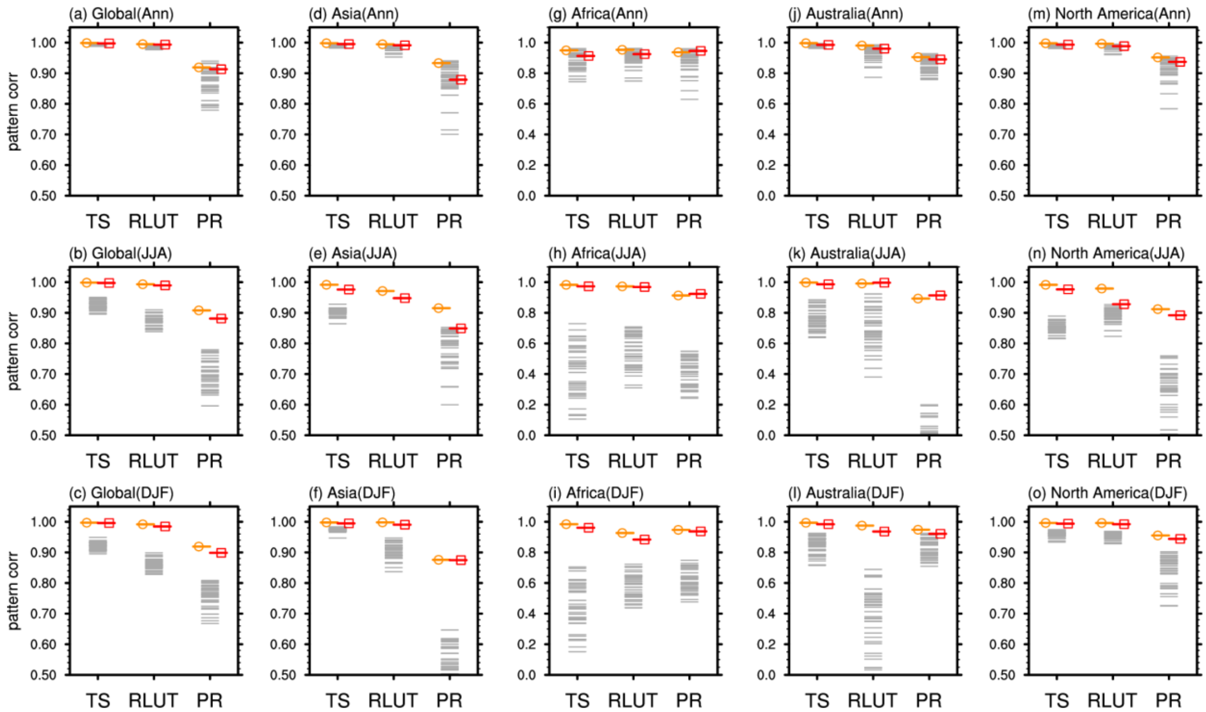

Figure 4: (a–o) Model ranking of pattern correlation annually (top) and in JJA (middle) and DJF (bottom) for (a—c) across the globe and four monsoon regions, including (d–f) Asia, (g–i) Africa, (j–l) Australia, and (m–o) North America, among surface temperature (TS), outgoing longwave radiation (RLUT), and precipitation (PR). The multiple model ensemble (MME) means of CMIP6 models are presented in orange, those of individual models are presented in gray, and that of TaiESM1 is presented in red. The four monsoon regions are annotated in Figure S1.

4.2 Seasonal evolution of monsoonal precipitation

The seasonal evolution of precipitation in the monsoon regions is presented in Figure 5: West Africa (20°W–30°E), South Asia (50°E–100°E), EAWNP (110°E–140°E), and Central America (110°W–50°W). As shown in Figures 5a–5c, TaiESM1 efficiently captures the seasonal evolution of the African monsoon (e.g., the northward advancement in spring, southward retreat in autumn, and peak in August), but with excessive tropical precipitation in April–June and November–December and slightly weaker precipitation in the peak period. However, the simulation of seasonal evolution in South Asia was less well simulated (Figures 5d–5f). Instead of simulating the northward advancement in spring and the southward retreat in autumn, the model simulated a relatively stationary precipitation pattern between 0°N and 20°N during June–August and a strong stationary rainband over the southern slope of the Himalayas and the Tibetan Plateau (25°N–30°N). These biases are consistent with the excessive precipitation south of the Indian subcontinent and the Tibetan Plateau displayed in Figure 3c; however, the reason for the biases is not well understood. One possibility is that the excessive precipitation south of the Tibetan Plateau, likely due to the oversimulated topographic effect in the region, induces anomalous subsidence over South Asia and prevents the development and northward advancement of precipitation. Another reason could be the undersimulated forcing of the Arakan Mountains in western Myanmar. Wu et al. (2014) reported that the deficiency in resolving the narrow north–south-elongated Arakan Mountains could lead to poor simulation of monsoon onset in the Bay of Bengal and underestimation of precipitation in the northeastern corner of the Bay of Bengal. The degree to which the topographic factors contribute to model biases requires further investigation.

For the EAWNP (110°E–140°E; Figures 5g–5i), achieving a realistic simulation of the asymmetric seasonal variation (e.g., strong/fast northward advancement and weak/slow southward retreat) by using climate models is often challenging. Each year, beginning in March, the EAWNP undergoes a series of transitions in precipitation (10°N–40°N in Figure 5g). The East Asian spring rain over subtropical East Asia (20°N–30°N) is followed by Mei-yu/Baiu and its northward migration in May–June. The termination of Mei-yu/Baiu in late July coincides with the onset of the WNP summer monsoon and typhoon season when the monsoon trough is established over the Philippine Sea and the subtropical anticyclonic ridge shifts suddenly northward. In September, the WNP monsoon begins a southward retreat (Chou et al., 2011; LinHo et al., 2008; Murakami & Matsumoto, 1994; Suzuki & Hoskins, 2009; Wu et al., 2009, 2018). The northward advancements in the stage-wise development of precipitation (Figure 5g), which is often a challenge for climate models to simulate, is well simulated in TaiESM1 (Figures 5g–5i). However, TaiESM still unrealistically simulated the split rainbands off of the equator during autumn and winter, which are associated with the double ITCZ model bias.

The model-simulated American monsoon (110°W–50°W) features presented in Figures 5j–5l indicates that the seasonal evolution was reasonably simulated by TaiESM1, with excessive precipitation during the evolution and dryness outside the precipitation region. Figure 5m presents the skills of the CMIP6 models to simulate the annual cycles (as shown in Figures 5a, 5d, 5g, and 5j) of four major monsoon regions during 1998–2014. The CMIP6 models (denoted by gray open circles) generally have good skill scores (i.e. >0.7) in the simulation of the seasonal evolution of precipitation in Africa, South Asia, East Asia, and Central America monsoonal regions. The CMIP6 ensemble mean (denoted by an orange cross) scored much higher (i.e. >0.9) than most models in all regions. TaiESM1 (denoted by a red cross) performed better than most CMIP6 models, especially over Africa and East Asia, with scores between 0.85 and 0.95.

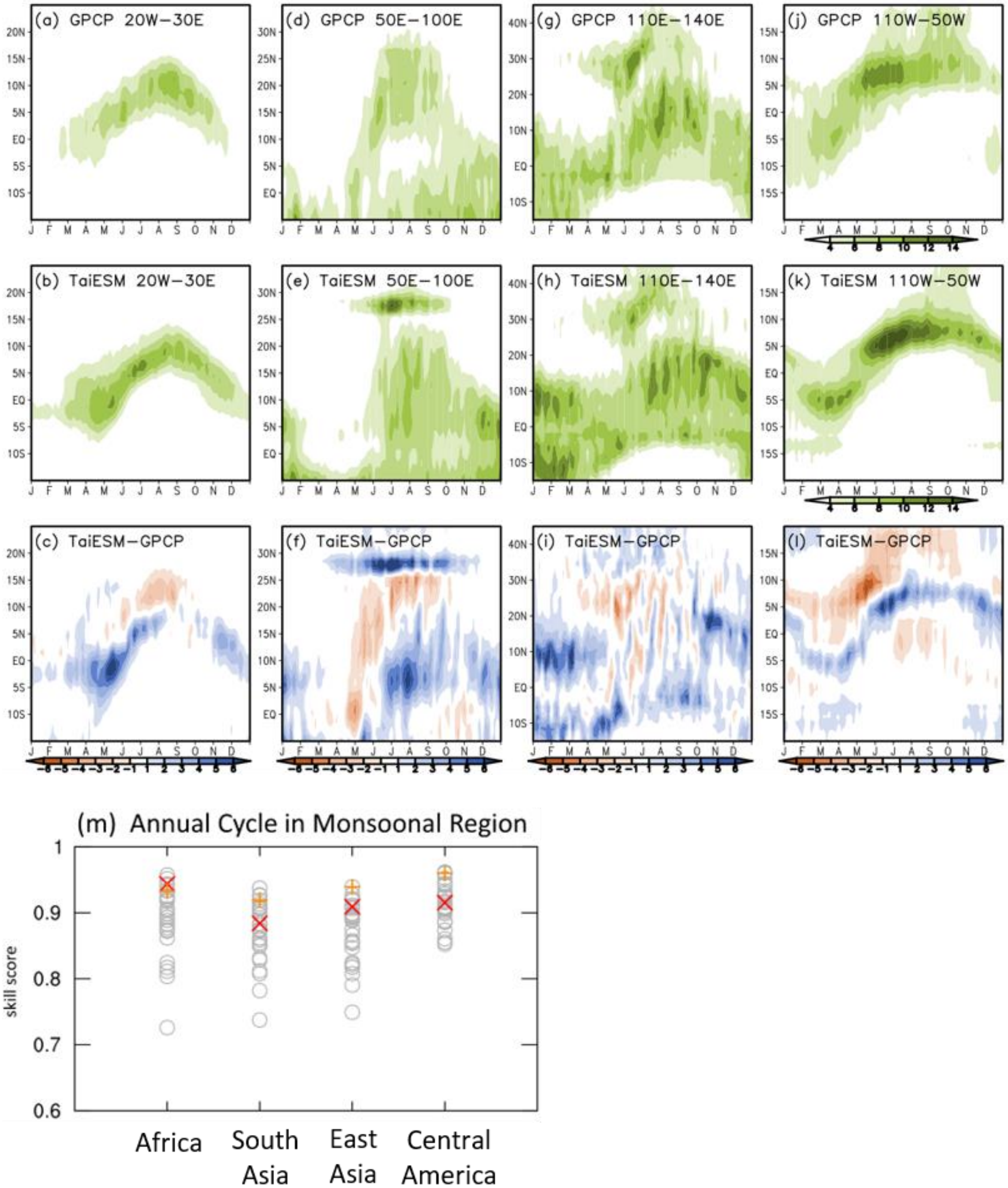

Figure 5. Latitude–time cross section of precipitation (mm day^{-1}, shading) obtained from observations from the GPCP and TaiESM1 and the differences between averages over regions (a–c) 20°W–30°E (Africa), (d–f) 50°E–100°E (South Asia), (g–i) 110°E–140°E (East Asia), and (j–l) 110°W–50°W (Central America) during 1998–2014. (m) Model ranking based on skill scores averaged over four monsoon regions with data simulated by TaiESM1 (red cross), CMIP6 models (gray circles), and the multimodel ensemble mean (orange plus).

5 Intraseasonal variability, synoptic variability, and extremes

5.1 Intraseasonal variability

The Madden–Julian Oscillation (MJO) is the dominant pattern of atmospheric intraseasonal (e.g., 20–100 days) variability in the tropics (Lau & Waliser, 2005; Madden & Julian, 1972; Zhang, 2005). MJO events are characterized by large-scale tropical circulation anomalies that develop over the Indian Ocean and propagate eastward into the western Pacific in 2–3 weeks. The summertime intraseasonal oscillation (ISO) is an important component of the Asian summer monsoon, which involves the movement of convection centers both northward and eastward in the equatorial and northern Indian Ocean and north-northwestward in the WNP (Hsu, 2005; Hsu & Weng, 2001; Lau & Chan, 1988). MJO events have major global impacts on monsoons, tropical storms, extratropical weather, and the ENSO. However, realistically representing the MJO by using the current climate models remains difficult (Hung et al., 2013; Kim et al., 2009, 2020). We evaluated the ability of TaiESM1 to simulate the MJO. The CLIVAR MJO Working Group diagnostics package was used to isolate and analyze intraseasonal variability (CLIVAR Madden-Julian Oscillation working group, 2009). Here, two seasons are defined: boreal winter (November to April) and boreal summer (May to October).

The wavenumber–frequency spectra of 850-hPa zonal wind averaged over 10°S–10°N simulated using TaiESM1 were compared with the observation spectra in Figure 6a. TaiESM1 simulated the observed wavenumber-1 structure with a much broader periodicity band and a maximum in the longer period (~80 days compared with the observed 30–80 days) during boreal winter (Figure 6a upper). This low-frequency tendency is reflected by the weaker and slower eastward propagation in the time-longitude Hovmöller diagrams (Figure 6b). Meridional propagation is one of the major characteristics of ISO. TaiESM1 simulated the observed northward propagation of the MJO over the northern Indian Ocean with slightly weaker strength but undersimulated the southward propagation tendency south of the equator (Figure 6c). The overall ISO performance of CMIP6 models, evaluated on the basis of the indices for the boreal winter and summer, is summarized in Figure 6d. In general, TaiESM1 tended to better simulate the overall amplitude of the intraseasonal variability but fairly simulated the propagation tendency (e.g., eastward/westward component ratio, W1, and northward propagation over NEQ S2) and periodicity of MJO.

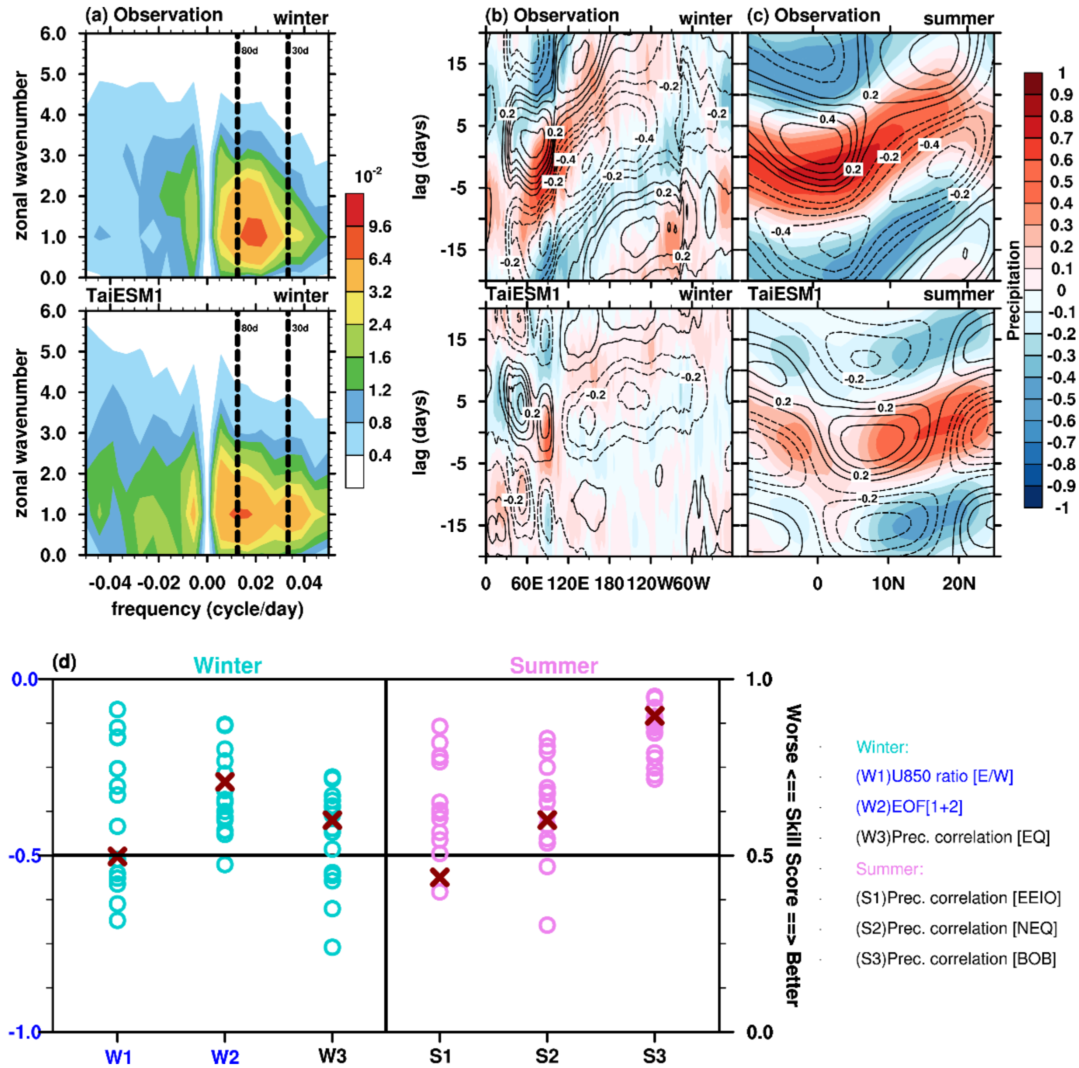

Figure 6. (a) Zonal wavenumber-frequency spectra for equatorial 850-hPa zonal wind between 10°S-10°N. Lag-longitude diagrams of intraseasonal rainfall (color) and 10-m zonal wind (contours) averaged over (b) 10°S-10°N correlated with Indian Ocean (10°S-5°N, 75°E -100°E) precipitation and (c) 80°E-100°E correlated with near equatorial region (5°N-10°N, 85°E -90°E) precipitation. (d) Summary diagram. Skill scores and the ratio of the 14 GCMs indicating their fidelity in representing the characteristics of MJO simulations. Each item is described in detail in the appendix. The left Y-axis shows units of W1 and W2, while the right Y-axis shows units of W3 and S1-S3. The cross denotes TaiESM1, and circles denote other CMIP6 models.

The efficiency of TaiESM1 in simulating the characteristics of convectively coupled equatorial waves over the tropical belt (30˚S–30˚N) has been assessed (Kiladis et al., 2009; Kim et al., 2009; Takayabu, 1994; Wheeler & Kiladis, 1999). Figures 7a and 7b show the space–time spectra of the symmetric component of equatorial precipitation following Wheeler and Kiladis (1999). The observation is characterized by strong variance associated with the MJO, equatorial

Kelvin and Rossby waves, and slightly weaker mixed Rossby–gravity waves. The simulation by TaiESM1 realistically represented these three main features but with weaker amplitudes. The Rossby waves and the high-frequency/high-wavenumber Kelvin waves were particularly weak. By contrast, the mixed Rossby–gravity waves were not realistically simulated. Following Dias and Kiladis (2014), we evaluated the model performance by season, and the results for the Kelvin and Rossby waves are presented in Figure 7c. A comparison of the annual eastward and westward wave spectra revealed that TaiESM1 exhibited higher skills than the other models, especially for westward propagation. In general, all models exhibited lower simulation skills in JJA and September-November (SON) and higher skills in March-May (MAM) and DJF. Notably, TaiESM1 exhibited higher skills for representing equatorial Rossby waves in DJF and MAM (i.e., index 07 and 10) compared with other models. This result is consistent with the high efficiency in simulating westward propagation (e.g., index 02).

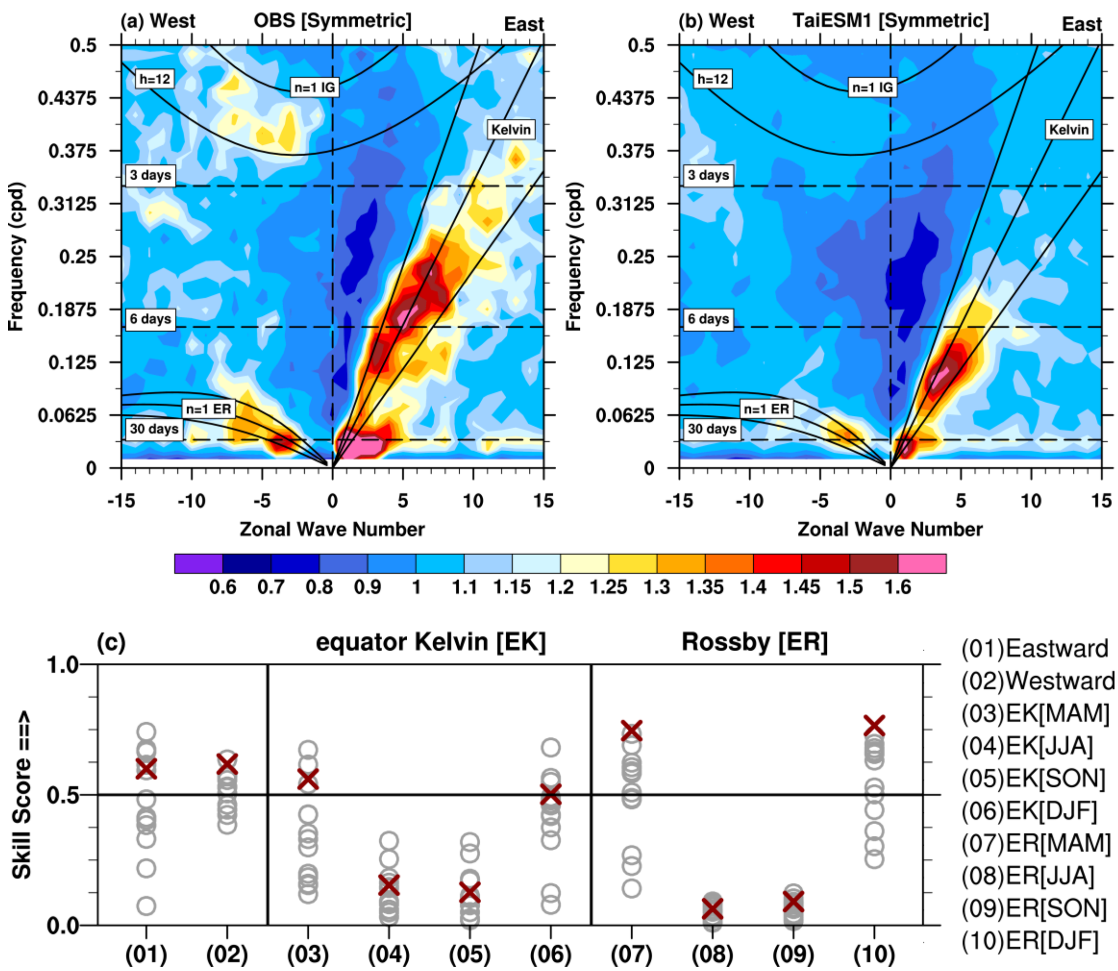

Figure 7: Symmetric coherence-squared in wavenumber-frequency spectrum between 15°S-15°N of precipitation in (a) observations and (b) TaiESM1 simulations. (c) Summary diagram. Skill scores and the ratio of the 14 GCMs indicating their fidelity in representing the characteristics of convective coupled equatorial waves in simulations. A

higher value indicates better simulation ability. Each item is explained in detail in the appendix. The cross indicates TaiESM1 and circles denote other CMIP6 models.

5.2 Synoptic eddy variability

Synoptic eddy activity causes daily temperature and precipitation fluctuation in the extratropics. The two-way energy conversion between the mean state and synoptic perturbations (i.e., the eddy–mean flow interaction) is a key physical process that keeps the balance between mean flows and synoptic eddies and helps maintain the atmospheric general circulation in the extratropics. For example, a synoptic eddy grows at the expense of the mean potential energy in the early stages of the lifecycle and feeds back kinetic energy to the mean flow in the later stages. A climate model that reasonably captures the aforementioned dynamic process and synoptic eddy activity is likely to more realistically simulate a mean state. Therefore, the model ability to simulate synoptic activity must be evaluated. In this study, synoptic perturbations were defined as 1–10-day bandpass-filtered fields such as wind and temperature.

Synoptic meridional momentum flux at 250 hPa and meridional heat flux at 850 hPa are important variables in kinetic and potential energy conversion, respectively, between the mean state and synoptic eddies and are often adopted as proxies to represent eddy activity. The observed 250-hPa meridional momentum flux in the Northern Hemisphere (Figure 8a) was maximized in the central North Pacific and North Atlantic around 30°N with an eastward extension to North America and Europe, respectively. In the Southern Hemisphere, the maxima appeared in the Southern Atlantic and Southern Indian Ocean around 40°S. The observed meridional heat flux at 850 hPa (not shown), which is often spatially and temporarily associated with momentum flux, was found mostly located to the westward and poleward side of the meridional momentum flux. The magnitudes and spatial distribution of these major features were realistically simulated by TaiESM1 (Figure 8c). A similar comparison for June–August also revealed the high performance of TaiESM1 in simulating the overall spatial distribution of eddy fluxes (not shown).

Despite fluctuating in a time scale of less than 10 days, the overall activity of synoptic eddies varies with a large-scale background environment such as the location and strength of jet streams and temperature gradient, which are strongly affected by known interannual fluctuations such as the ENSO. The interannual variance in meridional momentum for the observation and simulation is presented in Figures 8b and 8d. The interannual variance is defined as the variance of seasonal mean fluxes during 1975–2005. In the observation results, two major active regions of meridional momentum flux in the Northern Hemisphere were the eastern North Pacific and central North Atlantic (Figure 8b). The maxima of the meridional heat flux were found in the west of the maxima in the meridional momentum flux and in the east of Greenland with an eastward extension into the Eurasian Arctic. TaiESM1 reasonably simulated these features with weaker variance in both the North Pacific and Atlantic (Figure 8d). The variance of both fluxes in the Southern Hemisphere was also reasonably simulated but less skillful so compared with the simulation of the Northern Hemisphere. The spatial distribution during JJA was also realistically simulated (not shown). Overall, TaiESM1 could realistically simulate the spatial distribution and temporal (seasonal and interannual) fluctuation in synoptic eddy activity, thus demonstrating above average performance among the CMIP6 models (Figures 8e and 8f).

An interesting contrast in model performance is the overall lower pattern correlation (0.6–.07) for interannual variance in the Southern Hemisphere compared with the counterpart in the Northern Hemisphere (pattern correlation, ~0.8). The contrast in model performance reveals that even under the same forcing as the ENSO, the synoptic eddy activity in the Northern Hemisphere is easier to simulate than that in the Southern Hemisphere. The strong control of the significant land–sea contrast and topography in the North Hemisphere, which is absent in the Southern Hemisphere, is likely one of the major reasons.

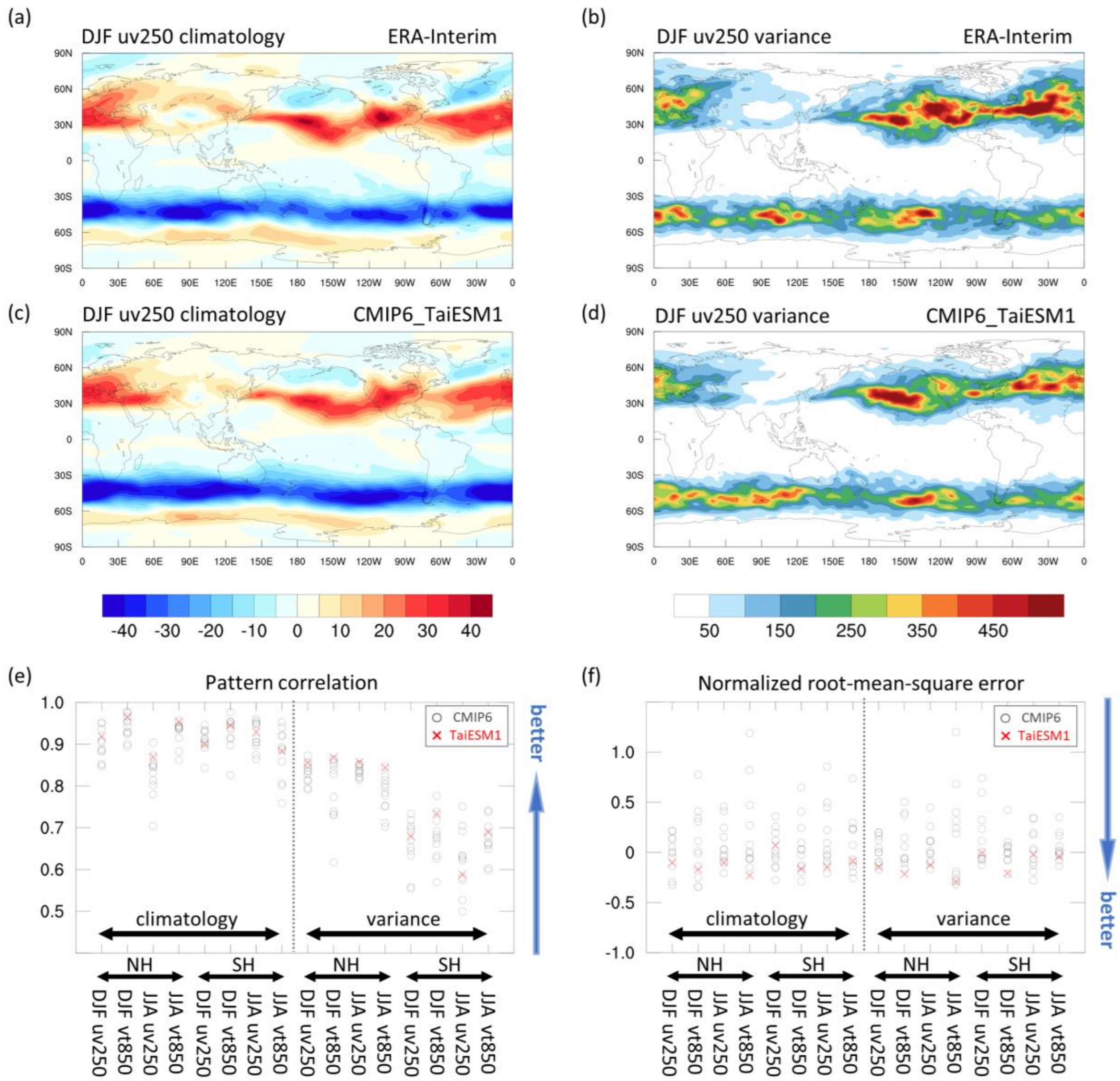

394

395 Figure 8. Performance of TaiESM1 in the simulation of synoptic eddy variability. (a, b) Observed and (c, d) simulated synoptic eddy momentum flux at 250 hPa during 1980/1981–2013/2014. DJF (a, c) climatology (m s^{-1}) and (b, d) interannual variance (m^2 s^{-2}). Pattern correlation (e) and normalized root-mean-square error (RMSE) (f) for synoptic eddy fluxes of 12 CMIP6 models (see Table S2). The seasonal mean climatology and interannual variance of the eddy momentum flux at 250 hPa (uv250) and eddy heat flux at 850 hPa (vt850) in the Northern Hemisphere storm track (NH, 15°N–75°N) and Southern Hemisphere storm track (SH, 30°S–60°S) during DJF and JJA were evaluated. Red crosses and gray circles represent TaiESM1 and other CMIP6 models, respectively. The medians of RMSEs are subtracted from the RMSEs, and the difference is then divided by the median. Smaller normalized RMSE values indicate higher performance.

5.3 Extreme precipitation events

We evaluated the performance of TaiESM1 by examining indices associated with extreme precipitation and compared the results with those of CMIP6 models. The skills of TaiESM1 and other models was evaluated against the precipitation indices derived from the 1-degree grid of the GPCP. The study region was the 40°S–40°N tropical belt during 1998–2014, considering the common data period of the GPCP and model outputs.

The indices of simple daily intensity (SDII), maximum 1-day precipitation (RX1day), maximum 5-day precipitation (RX5day), extreme precipitation intensity (PR99), total rainfall occurrence (TotFq, defined as daily precipitation exceeding 1 mm), and consecutive dry days (CDD) were analyzed to examine the representation of precipitation characteristics associated with extreme events.

To quantify the model performance against observations, the skill score S (Taylor, 2001) was calculated as follows:

$$\mathrm{S} = \frac{4(1+R)}{\left(\sigma + \frac{1}{\sigma}\right)^2 (1+R_0)},$$

where R represents the spatial pattern correlation coefficient between the observation and model simulation and σ is the ratio of the spatial standard deviation of the model simulation relative to that of the observation. R_0 is the maximum correlation attainable and is assumed to be 1 here.

To demonstrate the performance of TaiESM1 in simulating extreme indices, Figures 9a–9d displays the spatial pattern of RX1day in the GPCP and TaiESM1 as an example. Compared with the GPCP, TaiESM1 generally captures the seasonal main feature of RX1day in JJA (Figures 9a and 9c) and DJF (Figures 9b and 9d), despite some degree of overestimation or underestimation over the tropical region (e.g., overestimation in the EAWNP, eastern tropical Pacific, and southern Pacific regions and underestimation over Central Africa, Central America, and South America in JJA). Compared with the other CMIP6 models, TaiESM1 exhibited higher skill scores in the simulation of SDII, RX1day, RX5day, and PR99 in JJA and DJF (red cross in Figures 9e and 9f), similar to the performance in the CMIP6 ensemble. However, the scores associated with rainfall occurrence such as CDD and Totfq were relatively low. The models also tended to obtain lower scores when a lower threshold was selected for defining a wet day was selected (0.1 mm day^{-1}), indicating that the biases associated with too-frequent precipitation in previous model simulations (e.g., in CMIP phase 5) still existed in the sixth-generation CMIP models.

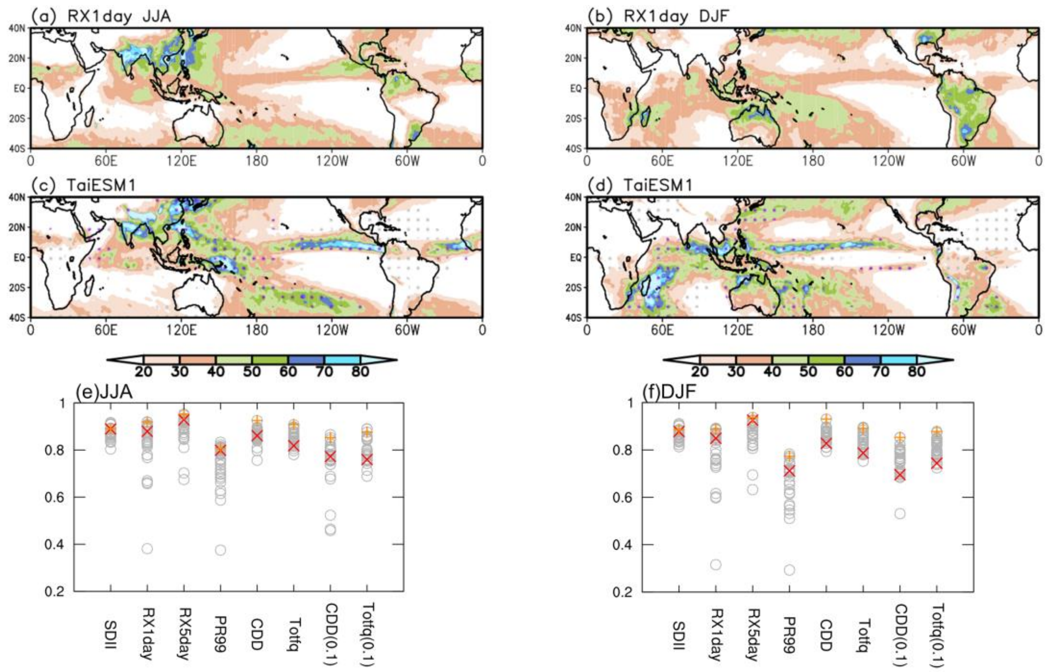

Figure 9. Spatial distribution of RX1day in (a) JJA and (b) DJF in the GPCP. (c and d) Same as (a and b), but for TaiESM1. The purple (gray) dotted region denotes the overestimated (underestimated) precipitation against the GPCP. (e and f) Model ranking based on the skill scores in simulating the extreme indices in JJA and DJF. CDD(0.1) and Totfq(0.1) represent the indices estimated using the wet-day definition of 0.1 mm day^{-1}.

We further examined the performance of TaiESM1 in simulating the extreme precipitation over the EAWNP region (115°E–135°E, 20°N–50°N). In the EAWNP region, the main wet season between the 28th and 54th pentad (i.e., May 16 to Sept 27) is divided into two rainy periods: the first wet season (1st_wet) is associated with the Mei-yu frontal system, and the second wet season (2nd_wet) is related to typhoon rainfall (Chen & Chen, 2003; Chen et al., 2019; Chou et al., 2009; Hsu et al., 2014; LinHo & Wang, 2002). The current General Circulation Models (GCM) are less skillful in simulating precipitation intensity during the Mei-yu season (Chen et al., 2019; Endo & Kitoh, 2016; Kusunoki, 2018; Kusunoki & Arakawa, 2015) and tropical cyclone activities (Flato et al., 2013; H. Murakami, Mizuta, et al., 2012; H. Murakami, Wang, et al., 2012), during which extreme precipitation is observed. Chen et al. (2020) compared the performance of CMIP5 and CMIP6 models in precipitation simulation in seasonal evolution and extreme indices in the EAWNP region. CMIP6 models generally have higher skill scores in the EAWNP region, which indicate their improvement over the CMIP5 models. As shown in Figures 10a–d, despite some degree of inconsistency, TaiESM1 could capture the spatial patterns associated with the Mei-yu rainband in the 1st_wet season and typhoon-related precipitation in the 2nd_wet season, which were similar to those obtained in the GPCP. TaiESM1 performs well in simulating the extreme indices in the EAWNP wet seasons (i.e. skill score > 0.6; Figures 10e–10f) and exhibited higher scores than most other CMIP6 models, especially in SDII, RX1day, RX5day, and PR99. These results indicate that the improvement in TaiESM1 might be mainly associated with the improved precipitation intensity rather than rainfall frequency. Model simulations in the EAWNP region presented errors associated with rainfall occurrence [i.e., CDD(0.1) and Totfq(0.1)], with more errors in the 1st_wet season than in the 2nd_wet season.

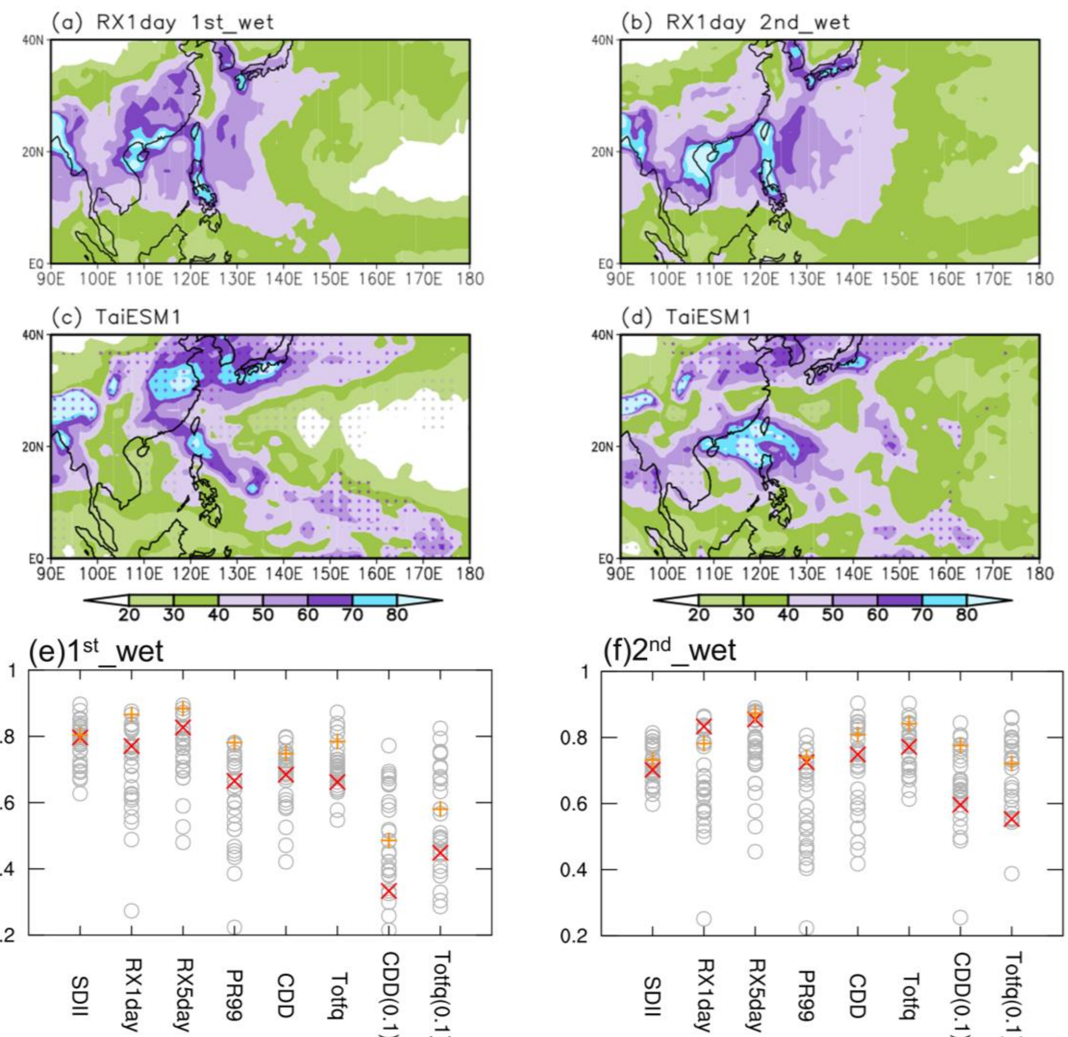

Figure 10. Spatial distribution of RX1day in the WNP-EA region (90°E–180°E, 0°N–40°N) in the (e) 1st_wet and (f) 2nd_wet seasons.

5.4 Diurnal rainfall phase and amplitude

The diurnal cycle denotes the prominent oscillation of a climate system forced by the diurnal variation of solar radiation. We conducted evaluations during the peak phase, which is the local time when diurnal rainfall peak occurs, and simulated the diurnal amplitude of the diurnal rainfall cycle by using TaiESM1 against the 3-hourly Tropical Rainfall Measurement Mission Multisatellite Precipitation Analysis (TMPA; Huffman et al., 2007) 3B42 observations. The evaluation was based on the first harmonic of the climatological diurnal rainfall cycle retrieved from the total data. We used data from 1998 to 2010 for TMPA and 30-year data for TaiESM1 historical runs. The phase and amplitude of diurnal rainfall in TaiESM1 shared similar biases as seen in other Atmosphere-Ocean GCMs (Figures 11a and 11b), including the underestimation of diurnal amplitude over the tropical lands and the early peaking time over most of the land region (Covey et al., 2016; Dai, 2006). However, unlike other models, TaiESM1 exhibited improved representations of the propagation behavior in the diurnal peak phase over many topographical regions and coastal regions, including the Southern Great Plains and the coastal regions of the maritime continent. This improvement result was also reported by Lee et al. (2020) and can be attributed to the improvements in the convective trigger function designs in TaiESM1 (Wang & Hsu, 2019). Figure 11c presents the performance of the CMIP6 model compared with TMPA observations based on the pattern correlation for the diurnal rainfall phase and amplitude. To compute the pattern correlation for the diurnal phase, the local phase was weighed with the local amplitude to determine the regions with stronger diurnal signals. The pattern correlation coefficients for amplitude and phase between TaiESM1 and TMPA observations were 0.68 and 0.69, respectively (Figure 11c). The performance of TaiESM1 in the amplitude simulation was above average compared with the other CMIP6 models (correlation, 0.5–0.8); however, TaiESM1 was demonstrated to be one of the best models for the simulation of diurnal phase distribution. The higher performance in the phase simulation can be attributed to the more efficient simulation in the rainfall propagation regions.

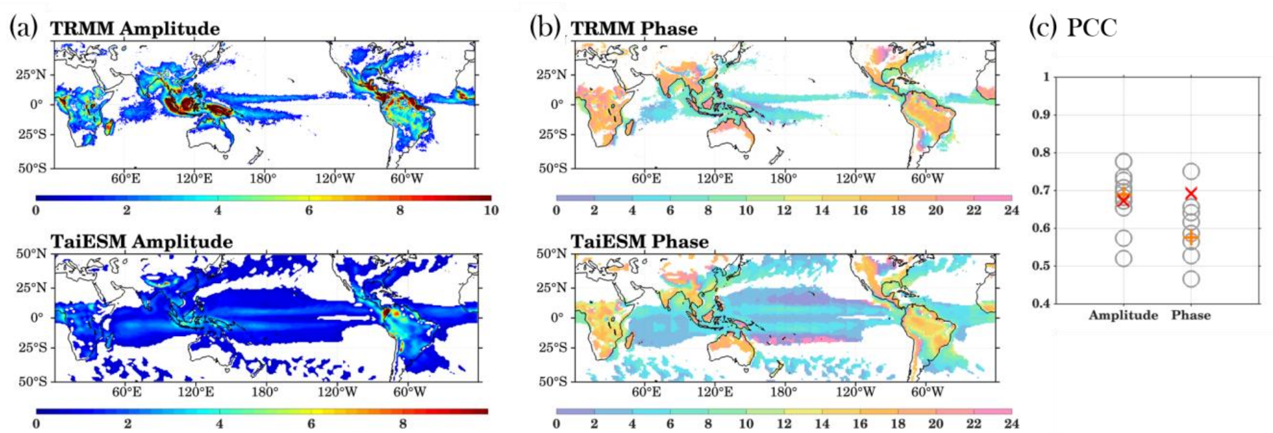

Figure 11. (a) Diurnal amplitude and (b) peak phase of TRMM 3B42 multisatellite products and historical run of TaiESM1. TRMM is regridded onto the 0.9° × 1.25° grid of TaiESM1 for comparison. (c) Model ranking based on pattern correlations of phase and amplitude. The pattern correlation of phase is only considered for regions with diurnal amplitudes greater than 1.2 mm/day, which approximately equates the global mean of diurnal amplitude. The results of TaiESM1 are denoted by red crosses, medians are denoted by orange pluses, and the results of the CMIP6 models are denoted by gray circles.

6 Interannual–interdecadal variability

6.1 El Niño–Southern Oscillation

The ENSO is one of the most prominent phenomena that contribute significantly to interannual variability. Like the MJO, realistic simulation of the ENSO by using climate models is challenging. To construct model-simulated ENSO composite, we identified the strong ENSO events simulated with the Nino3.4 index larger than 1.5 standard deviation of the entire period. Five ENSO events are then identified from the TaiESM simulation and used for the composite. Figure 12 presents the spatial distributions of surface temperature, mean sea-level pressure, and 1000-hPa wind anomalies in December–February when the ENSO is in the mature stage; they are based on the composites of five El Niño events by TaiESM1 (Figure 12a) and their differences from the composites of six events in the MRE2 dataset (Figure 12b). The TaiESM1-simulated SST anomaly (SSTA) was evidently larger in terms of both amplitude and covered area than the observed values, and the maximum shifted westward to the central equatorial Pacific compared with observations (Figure 12a), which is a common bias seen in many climate models (Bellenger et al., 2014). The horseshoe-like negative SSTA in the northwest/southwest and west of the positive SSTA correspondingly shifted westward compared with observations and exhibited a cold bias in the far western tropical Pacific (Figure 12b). This overestimated SSTA structure led to marked biases in the simulated atmospheric circulation and temperature. The biased strong SSTA induced a stronger-than-observation near-surface convergence toward the central equatorial Pacific. In response to the westward shift of positive SSTA in the equator, the circulation and temperature anomaly patterns shifted westward. For example, the westward-shifted western Pacific anticyclonic anomaly and the observed warm–cool SSTA dipole in the subtropical WNP during El Niño induced by the local atmosphere–ocean interaction (Wang et al., 2000) was not efficiently simulated. The region is dominated by negative SSTA, with the positive SSTA restricted over the coastal East Asia. The cool–warm structure in extratropical Asia seen in observations shifted westward toward the interior of the Asian continent in the simulation. The warming in the Indian Ocean, which often occurs following the onset of El Niño, also occurred to the west of the observed location together with the westward shift of the anticyclonic circulation anomaly in the Southern Indian Ocean. The observed northwesterly anomaly to the west of Australia was seen as a southwesterly anomaly in the simulation, which evidently induced upwelling and cooler temperatures along the Australian west coast. By contrast, the temperature and circulation over North America and the North Atlantic were more realistically simulated; however, the Bering Sea was warmer and the northwestern North America was cooler than the observed temperatures.

Figure 12c presents the observed and simulated spectra of the Niño 3.4 index. The observed Niño 3.4 index exhibited three statistically significant peaks between 2 and 8 years. TaiESM1 simulated a strong spectral peak at approximately 4–5 years and another strong peak at approximately 8 years. El Niño simulated by TaiESM1 had a larger amplitude than that simulated by most of the CMIP6 models (e.g., exceeding the 75th percentile of CMIP6 models, dashed line in Figure 12c), which likely led to the large extratropical responses displayed in Figure 12a. The spectra of all CMIP6 models indicated a wide range of ENSO amplitudes among CMIP6 models (grey shading in Figure 12c). Figure 12d presents the skill scores of the models in simulating the observed El Niño SST in the tropical Pacific for four seasons preceding and following the peak of El Niño. The performance of TaiESM1 was among the best, except in DJF+1 when El Niño was in its peak. The CMIP6 models tended to perform poorly in the spring (MAM+1) following the peak phase of El Niño.

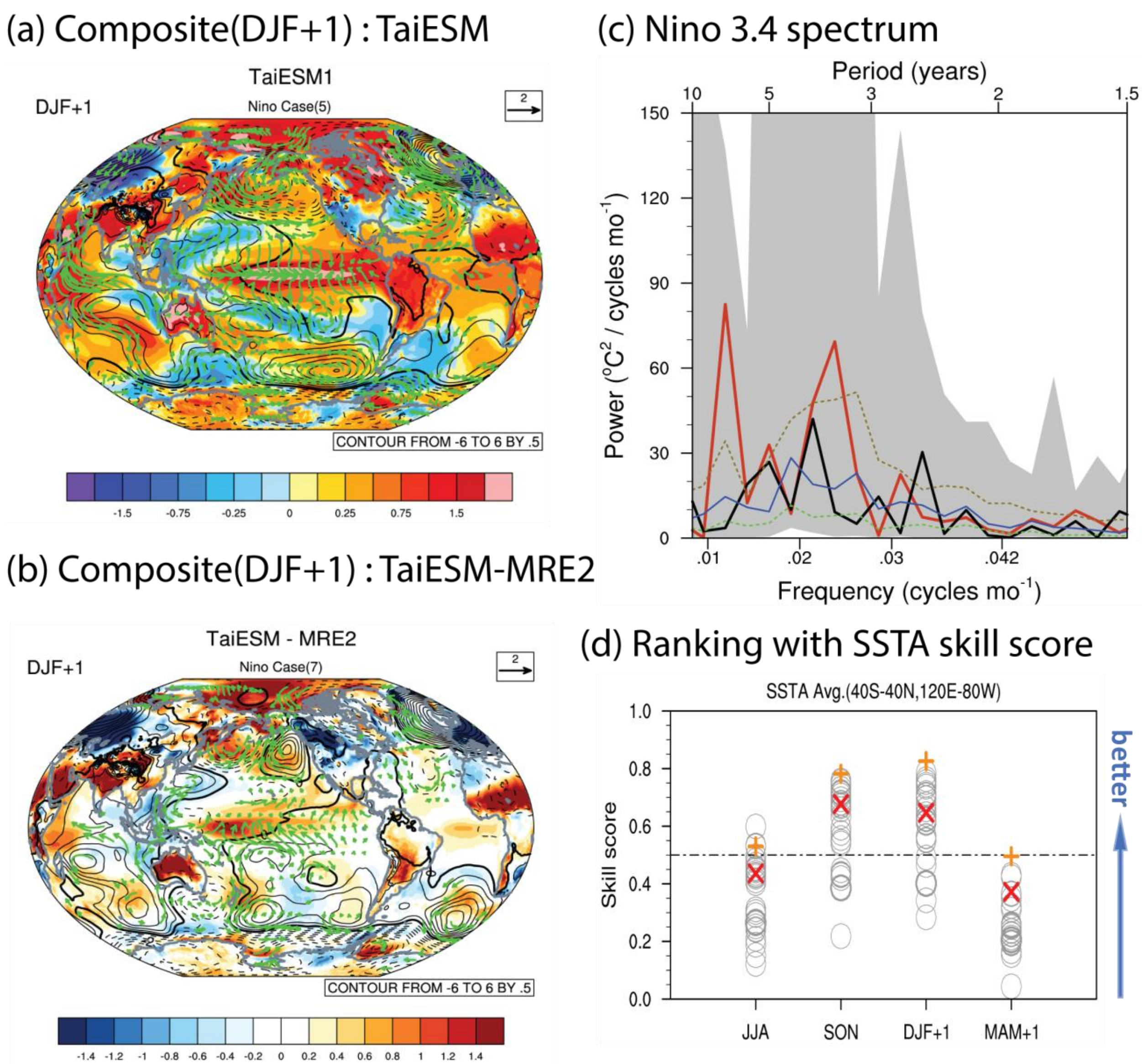

Figure 12. Spatial composites of surface temperature (shading), mean sea-level pressure (contours), and 1000-hPa wind anomalies (green arrows) of ENSO for (a) TaiESM1 and (b) differences between TaiESM1 and MRE2 reanalysis ensemble. (c) Spectrum of Nino 3.4 from TaiESM1 (red), observations (black), and a range of CMIP6 models (25%: green, median: blue dashed lines, 75%: brown dashed lines, gray shading). (d) Normalized skill scores of geological patterns obtained from TaiESM1, multimodel ensemble, and CMIP6 models (big circles) compared with the MRE2 ensemble in the winter season. They are normalized on the basis of the median member of all CMIP6 models.

6.2 Atlantic Multidecadal Oscillation and Pacific Decadal Oscillation

Oceanic interdecadal–multidecadal fluctuations are considered the major reason for climate variability beyond interannual time scales. Two well-known oscillations beyond the decadal time scale, the AMO and PDO, were identified for further evaluation of the TaiESM1.

A comparison between observed PDO and PDO simulated by TaiESM1 is presented in Figures 13a and 13b. The overall simulated pattern was similar to that of the observation: a negative SSTA in the extratropical North Pacific, a horseshoe-like positive SSTA in the extratropical eastern Pacific, and a positive SSTA in the equatorial central–eastern Pacific. The weaker SSTA structure in the other oceans was also simulated. However, consistent with the bias in the El Niño simulation, the positive and negative SSTA in the equatorial Pacific shifted to the west of the observed pattern. The Taylor diagram presented in Figure 13c reveals that all CMIP6 models exhibited a pattern correlation between 0.8 and 0.9 and large disagreements in terms of mode variability. TaiESM1 exhibited a correlation of 0.9 and a variability ratio of approximately 1.25, which is at the upper end of that of the CMIP6 models. This bias is consistent with the strong ENSO signal simulated by TaiESM1.

Figures 13d–13f display the observed and simulated AMO, which significantly affects the regional and global climate. The major centers of SSTA in the extratropical North Atlantic, tropical Atlantic, central/eastern equatorial Pacific, and extratropical Pacific were realistically simulated by TaiESM1 (Figures 13d and 13e). Figure 13f shows that the performance of TaiESM1 in AMO simulation was average, with a correlation of 0.7, compared with a correlation range of 0.6–0.85 among the CMIP6 models.

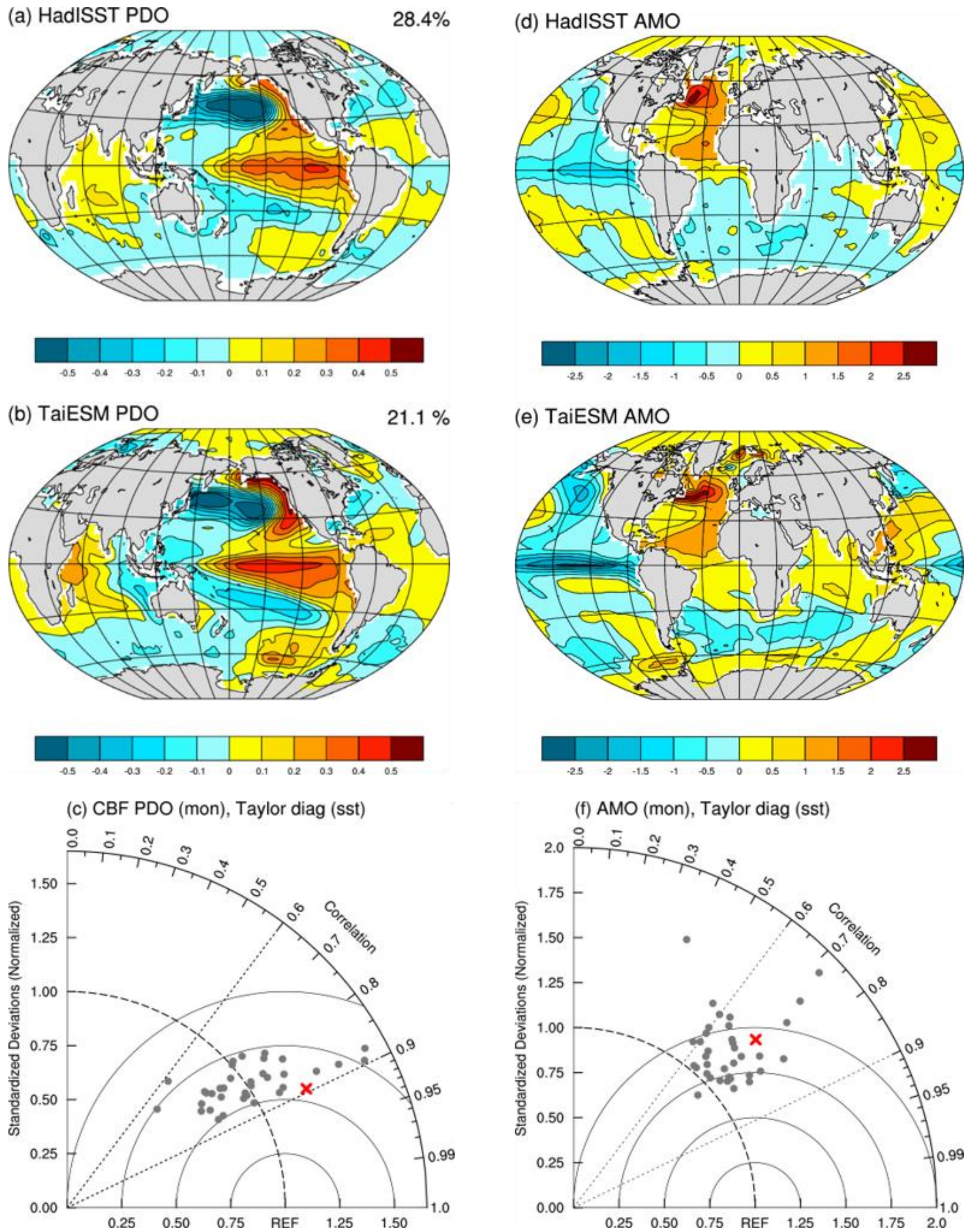

Figure 13. (a–c) Geospatial patterns of Pacific Decadal Oscillation (PDO) derived from HadISST and TaiESM1 and Taylor diagrams between the two modes. (d–f) Similar comparison as (a–c) for the Atlantic Multidecadal Oscillation (AMO) between HadISST and TaiESM1.

6.3 Atmospheric teleconnection

Atmospheric teleconnections are important phenomena that link climate variation in separate remote regions, thereby influencing regional climates. Therefore, climate models should be able to accurately simulate the main characteristics of teleconnection patterns to produce a reasonable global climate variability distribution. The performance of TaiESM1 in simulating well-known teleconnection patterns was evaluated. We adopted the CBF method to extract climate modes of models to avoid problems such as mode swapping. This is important for regional modes, such as the Pacific–Japan (PJ) pattern, which appears as the leading EOF in MRE2 precipitation (110°E–180°, 5°N–55°N; similar structure in the GPCP, not shown), with a tripolar structure, but as the second EOF in TaiESM1.

Figure 14 presents the spatial structures of the Arctic Oscillation (AO; Thompson & Wallace, 1998) in winter and the PJ pattern (Hsu & Lin, 2007; Kosaka & Nakamura, 2006; Nitta, 1987) in summer as examples. Observations and simulations of the AO, which is defined as the first EOF of seasonal mean sea-level pressure north of 20°N, are shown in Figures 14a and 14b, respectively. The out-of-phase relationship between the polar region and middle latitudes and the location of major centers were reasonably simulated by TaiESM1. However, the Atlantic component of the meridional dipole was weakly simulated, whereas the simulation of the Pacific component was stronger than the observation. The explained variance in simulation was approximately 33.4%, which is very close to the observed 33.5%. For the PJ pattern, TaiESM1 realistically simulated the out-of-phase pattern between north and south parts of the East Asia region seen in the observations (Figures 14c and 14d). Although the locations of the maximum were captured, TaiESM1 has a stronger simulated amplitude and a higher explained variance of 25.6% compared with the 24.6% of variance explained by observations.

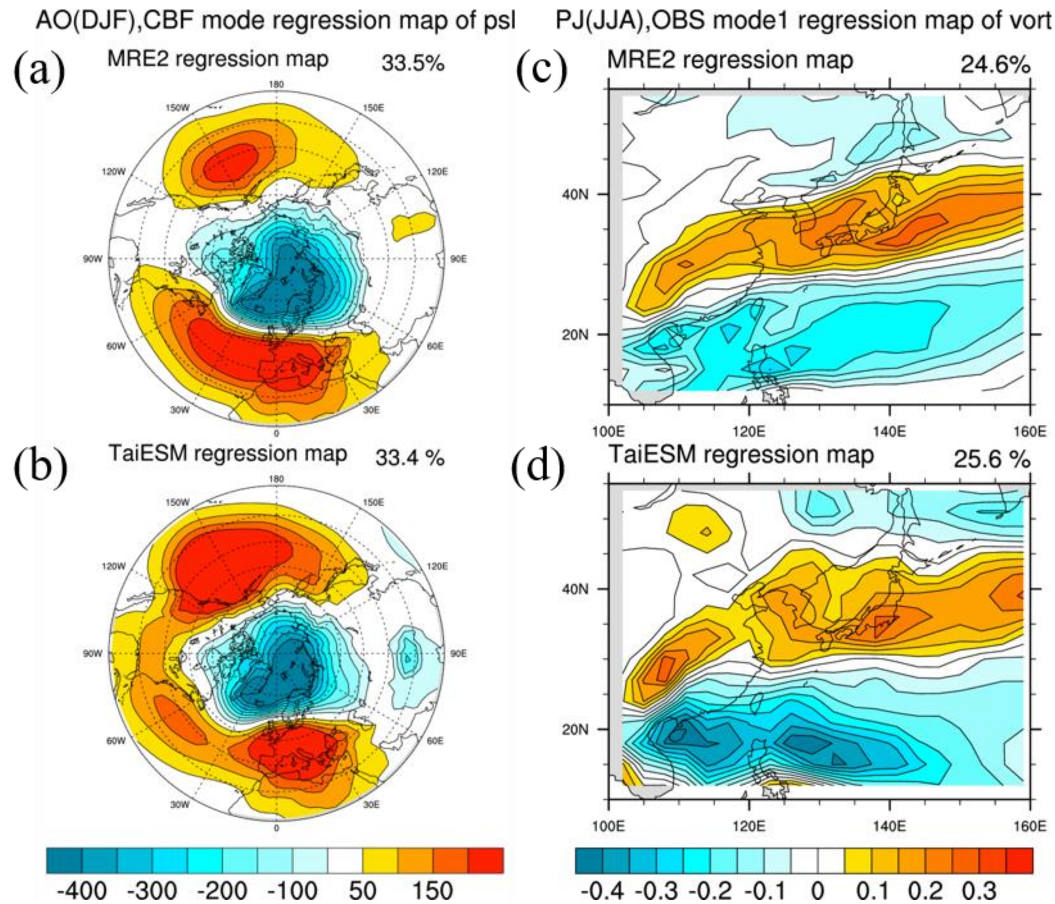

Figure 14. (a and b) Geospatial patterns of the Arctic Oscillation (AO) and (c and d) Pacific Japan (PJ) between MRE2 and TaiESM1.

Figure 15 presents the Taylor diagrams of four important teleconnections, namely the AO, PJ, and PNA (Wallace & Gutzler, 1981) patterns, and the North Atlantic Oscillation (NAO; vanLoon & Rogers, 1978; Rogers & vanLoon, 1979; Walker & Bliss, 1932) obtained by all CMIP6 models and TaiESM1, on the basis of the CBF method. The Taylor diagram for AO shows that TaiESM1 realistically simulated the AO (red cross) like most CMIP6 models did, with a pattern correlation greater than 0.9 (Figure 15a). As displayed in Figure 15b, the simulated PJ pattern in TaiESM1 had a pattern correlation of 0.85 with the observed pattern, whereas the CMIP6 models had correlations of 0.8–0.9. The PNA and NAO are two dominant atmospheric intrinsic modes of seasonal and interannual variability and influence interdecadal and longer time scales through interactions with oceans (Battisti et al., 2019). For simulating the PNA pattern (Figure 15c), the TaiESM1 was the second best among the CMIP6 models, with a pattern correlation of 0.96 and an amplitude very close to the observation. Most models simulated the NAO pattern well, with a pattern correlation ranging between 0.85 and 0.9 (Figure 15d). TaiESM1 reasonably simulated the NAO, with a pattern correlation of 0.85. These results indicate the high reproducibility of observed teleconnection patterns in TaiESM1. Notably, the CMIP6 models exhibited a similar ability to simulate the major atmospheric modes but had a greater degree of variance. TaiESM1 is also one of the models with the best performance in terms of normalized RMSE and the ratio of variability relative to the observations.

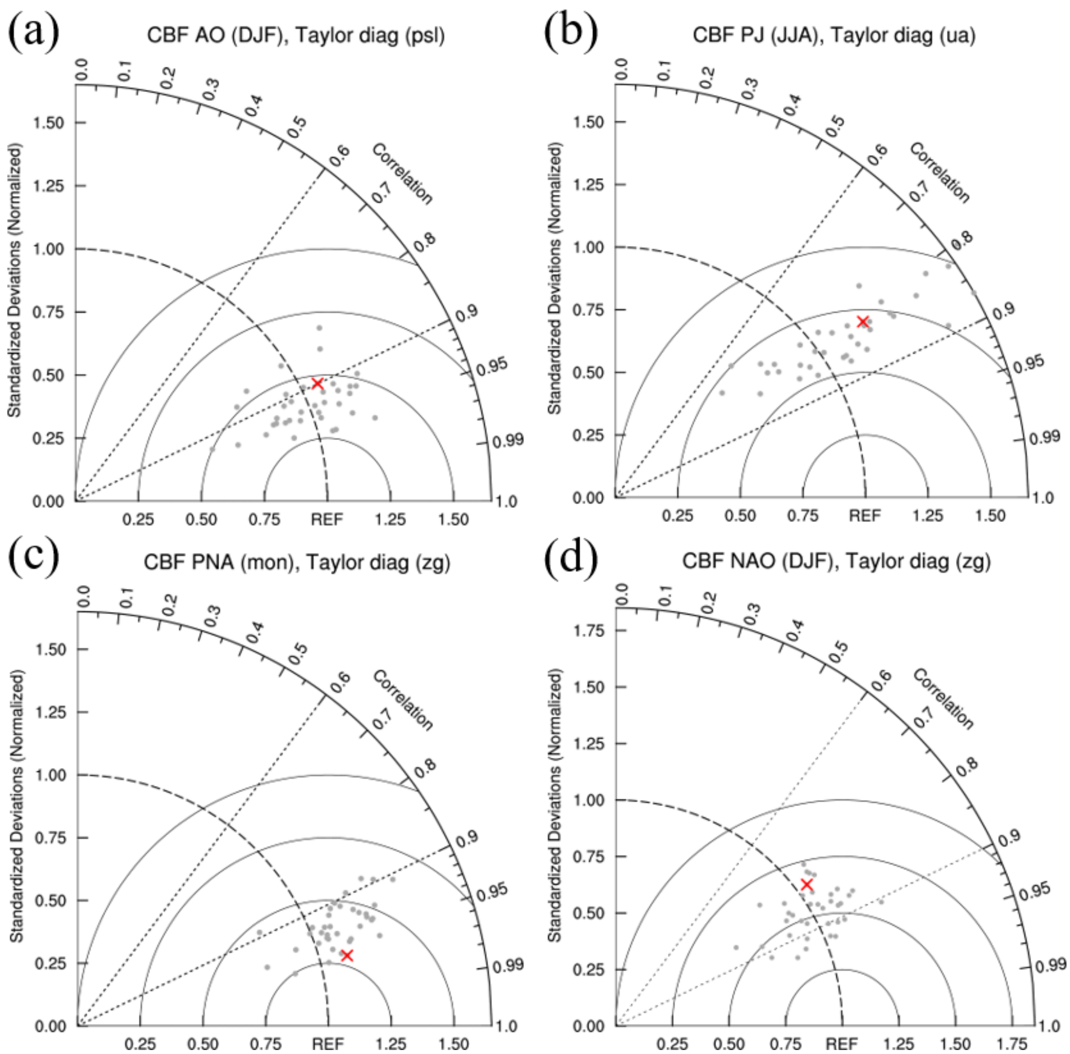

Figure 15. Taylor diagrams for evaluating important geographical features of teleconnection obtained using CMIP6 models. (a) The Arctic Oscillation (AO) in DJF, (b) Pacific Japan pattern in JJA, (c) Pacific North American Oscillation (PNA), and (d) North Atlantic Oscillation (NAO) in DJF among TaiESM1 (red cross), CMIP6 models (gray dots), and the MRE2 ensemble. Evaluations are based on regressed spatial patterns of sea-level pressure with the AO, PNA, and NAO and vorticity with PJ between TaiESM1 and MRE2.

7 Discussion and conclusions

This study evaluated the performance of TaiESM1 in simulating the observed climate variability in the historical simulation driven by CMIP6 forcing. TaiESM1 was developed on the basis of CESM1.2.2, with modifications to the cumulus convection scheme and cloud fraction scheme, replacement of the aerosol scheme with a new one, and implementation of a unique scheme for three-dimensional surface absorption of shortwave radiation that resolves the effects of complex terrains on the surface radiation budget. Most model valuations focus on the climatological mean, whereas TaiESM1 focuses on climate variability, including precipitation extremes, synoptic eddy activity, intraseasonal fluctuation, monsoon evolution, and interannual and multidecadal atmospheric and oceanic teleconnection patterns. The series of intercomparisons between the simulations of TaiESM1 and CMIP6 models and observations indicate that TaiESM1, is capable of realistically simulating the observed climate variability at various time scales and is favorable to the CMIP6 models in terms of many key climate features. Biases were also identified and discussed.

We also estimated the equilibrium climate sensitivity (ECS) to characterize the surface warming of TaiESM in response to increasing greenhouse gas emissions. Compared with CMIP5, CMIP6 models are reported to have an even larger range of ECS between 1.8℃ and 5.6℃ (Meehl et al., 2020). To better interpret future climate changes projected under various emission scenarios, the range of model sensitivity should be understood. We used the method proposed by Gregory et al. (2004), which contrasts the residual energy and surface temperature obtained from the $4 \times CO_2$ (years 1–150) and the preindustrial (years 501–650) experiments to evaluate the ECS of TaiESM1 (Figure 16a). Compared with the ECS calculated by Zelinka et al. (2020; Table S1), the ECS of TaiESM1 was 4.32℃, which is higher than the average of 3.8℃ among the CMIP6 models (Figure 16b). The CMIP6 models were considerably more sensitive than the CMIP5 models (Zelinka et al., 2020). The sensitivity of TaiESM1 is at the 59th percentile among the CMIP6 models.

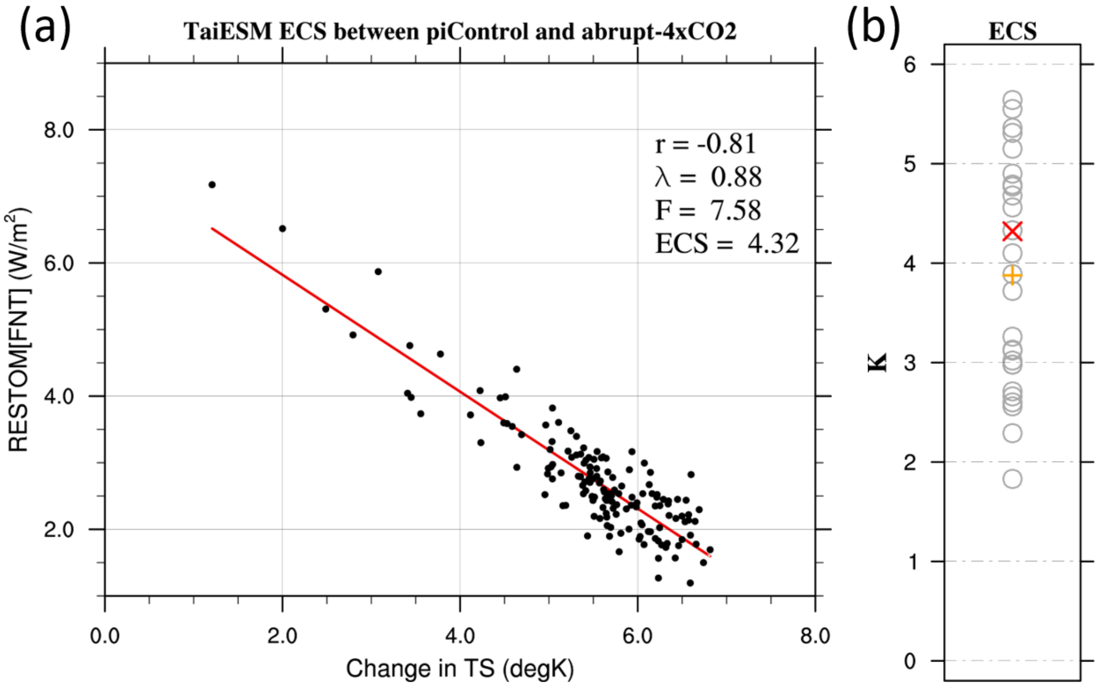

Figure 16. (a) Scatter plot of changes in the top-of-atmosphere energy residual and surface temperatures in TaiESM1 between the 4 × CO_2 (years 1–150) and preindustrial (years 501–650) experiments for estimating equilibrium climate sensitivity (ECS). ECS = −intercept/2 × slope of the regression line in (a), following Gregory et al. (2004). (b) Model spread for ECS among CMIP6 models. TaiESM1 is denoted by a red cross; CMIP6 models are denoted by gray circles, and their median members are denoted by an orange plus. The ECSs of the CMIP6 models in Zelinka et al. (2020) were plotted for comparison.

TaiESM1 is a participating climate model in the CMIP6 and has provided independent simulations and outputs for the Diagnostic, Evaluation and Characterization of Klima experiments and model intercomparison projects (MIPs) such as the Scenario MIP, Global Monsoon MIP, Aerosol/Chemistry MIP, and Cloud Forcing MIP, which are available at the data portal (https://doi.org/10.22033/ESGF/CMIP6.9684). Through CMIP6 and preparation for the upcoming Sixth Climate Change Assessment report of the Intergovernmental Panel for Climate Change, TaiESM1 will join the efforts to expand our understandings of variability and changes of the earth system with the global scientific community.

Acknowledgments, Samples, and Data

This study was conducted under the Consortium for Climate Change Study and was supported by grants from the Ministry of Science and Technology, Taiwan (MOST 109-2123-M-001-004 and

MOST 105-2119-M-001-018). All observational data sets used in this study are available online, and a complete list of download sites and literature is included in the supplementary materials. The data used to produce Figure 15b are based on the data provided in the supplementary materials of Zelinka et al. (2020). A complete list of the CMIP6 model data used in this study can also be found there. All CMIP6 model data presented in this research, including for TaiESM1, can be downloaded from the data portal for CMIP6 hosted by Lawrence Livermore National Laboratory, Department of Energy (http://esgf-node.llnl.gov/search/cmip6/). We extend special thanks to the National Center for High Performance Computing for their computational support for TaiESM1 development and participation in CMIP6 activity.

References

Adler, R. F., Huffman, G. J., Chang, A., Ferraro, R., Xie, P.-P., Janowiak, J., et al. (2003). The Version-2 Global Precipitation Climatology Project (GPCP) Monthly Precipitation Analysis (1979–Present). *Journal of Hydrometeorology*, *4*(6), 1147–1167. https://doi.org/10.1175/1525-7541(2003)004<1147:TVGPCP>2.0.CO;2

Battisti, D. S., Vimont, D. J., &Kirtman, B. P. (2019). 100 Years of Progress in Understanding the Dynamics of Coupled Atmosphere–Ocean Variability. *Meteorological Monographs*, *59*, 8.1-8.57. https://doi.org/10.1175/AMSMONOGRAPHS-D-18-0025.1

Bellenger, H., Guilyardi, E., Leloup, J., Lengaigne, M., &Vialard, J. (2014). ENSO representation in climate models: from CMIP3 to CMIP5. *Climate Dynamics*, *42*(7–8), 1999–2018. https://doi.org/10.1007/s00382-013-1783-z

Chen, C.-A., Hsu, H. H., &Liang, H. C. (2020). Evaluation and Comparison of CMIP6 and CMIP5 Model Performance in Simulating the Seasonal Extreme Precipitation in the Western North Pacific and East Asia.

Chen, C.-S., &Chen, Y.-L. (2003). The Rainfall Characteristics of Taiwan. *Monthly Weather Review*, *131*(7), 1323–1341. https://doi.org/10.1175/1520-0493(2003)131<1323:TRCOT>2.0.CO;2

Chen, Chao-An, Hsu, H.-H., Hong, C.-C., Chiu, P.-G., Tu, C.-Y., Lin, S.-J., &Kitoh, A. (2019). Seasonal precipitation change in the Western North Pacific and East Asia under global warming in two high-resolution AGCMs. *Climate Dynamics*, *53*(9–10), 5583–5605. https://doi.org/10.1007/s00382-019-04883-1

Chen, J.-P., Tsai, I.-C., &Lin, Y.-C. (2013). A statistical–numerical aerosol parameterization scheme. *Atmospheric Chemistry and Physics*, *13*(20), 10483–10504. https://doi.org/10.5194/acp-13-10483-2013

Chou, C., Huang, L.-F., Tseng, L., Tu, J.-Y., &Tan, P.-H. (2009). Annual Cycle of Rainfall in the Western North Pacific and East Asian Sector. *Journal of Climate*, *22*(8), 2073–2094. https://doi.org/10.1175/2008JCLI2538.1

Chou, M.-D., Wu, C.-H., &Kau, W.-S. (2011). Large-Scale Control of Summer Precipitation in Taiwan. *Journal of Climate*, *24*(19), 5081–5093. https://doi.org/10.1175/2011JCLI4057.1

CLIVAR Madden-Julian Oscillation working group. (2009). MJO Simulation Diagnostics. *Journal of Climate*, *22*(11), 3006–3030. https://doi.org/10.1175/2008JCLI2731.1

Covey, C., Gleckler, P. J., Doutriaux, C., Williams, D. N., Dai, A., Fasullo, J., et al. (2016). Metrics for the diurnal cycle of precipitation: Toward routine benchmarks for climate models. *Journal of Climate*, *29*(12), 4461–4471. https://doi.org/10.1175/JCLI-D-15-0664.1

Dai, A. (2006). Precipitation Characteristics in Eighteen Coupled Climate Models. *Journal of Climate*, *19*(18), 4605–4630. https://doi.org/10.1175/JCLI3884.1

Dias, J., &Kiladis, G. N. (2014). Influence of the basic state zonal flow on convectively coupled equatorial waves. *Geophysical Research Letters*, *41*(19), 6904–6913. https://doi.org/10.1002/2014GL061476

Endo, H., &Kitoh, A. (2016). Projecting Changes of the Asian Summer Monsoon Through the Twenty-First Century (pp. 47–66). https://doi.org/10.1007/978-3-319-21650-8_4

Eyring, V., Bony, S., Meehl, G. A., Senior, C. A., Stevens, B., Stouffer, R. J., &Taylor, K. E. (2016). Overview of the Coupled Model Intercomparison Project Phase 6 (CMIP6) experimental design and organization. *Geoscientific Model Development*, *9*, 1937–1958. https://doi.org/10.5194/gmd-9-1937-2016

Flato, G., Marotzke, J., Abiodun, B., Braconnot, P., Chou, S. C., Collins, W., et al. (2013). Evaluation of Climate Models. *Climate Change 2013: The Physical Science Basis. Contribution of Working Group I to the Fifth Assessment Report of the Intergovernmental Panel on Climate Change*, 741–866. https://doi.org/10.1017/CBO9781107415324

Gleckler, P. J., Taylor, K. E., &Doutriaux, C. (2008). Performance metrics for climate models. *Journal of Geophysical Research*, *113*(D6), D06104. https://doi.org/10.1029/2007JD008972

Gregory, J. M., Ingram, W. J., Palmer, M. A., Jones, G. S., Stott, P. A., Thorpe, R. B., et al. (2004). A new method for diagnosing radiative forcing and climate sensitivity. *Geophysical Research Letters*, *31*(3), L03205. https://doi.org/10.1029/2003GL018747

Hsu, H.-H. (2005). East Asian monsoon. In W. K. M.Lau &D. E.Waliser (Eds.), *Intraseasonal Variability in the Atmosphere-Ocean Climate System* (pp. 63–94). Berlin, Heidelberg: Springer Berlin Heidelberg. https://doi.org/10.1007/3-540-27250-X_3

Hsu, H.-H., &Lin, S.-M. (2007). Asymmetry of the Tripole Rainfall Pattern during the East Asian Summer. *Journal of Climate*, *20*(17), 4443–4458. https://doi.org/10.1175/JCLI4246.1

Hsu, H.-H., &Weng, C.-H. (2001). Northwestward Propagation of the Intraseasonal Oscillation in the Western North Pacific during the Boreal Summer: Structure and Mechanism. *Journal* *of Climate*, *14*(18), 3834–3850. https://doi.org/10.1175/1520-0442(2001)014<3834:NPOTIO>2.0.CO;2

Hsu, H.-H., Zhou, T., &Matsumoto, J. (2014). East Asian, Indochina and Western North Pacific Summer Monsoon - An update. *Asia-Pacific Journal of Atmospheric Sciences*, *50*(1), 45–68. https://doi.org/10.1007/s13143-014-0027-4

Huffman, G. J., Bolvin, D. T., Nelkin, E. J., Wolff, D. B., Adler, R. F., Gu, G., et al. (2007). The TRMM Multisatellite Precipitation Analysis (TMPA): Quasi-Global, Multiyear, Combined-Sensor Precipitation Estimates at Fine Scales. *Journal of Hydrometeorology*, *8*(1), 38–55. https://doi.org/10.1175/JHM560.1

Huffman, G. J., Adler, R. F., Bolvin, D. T., &Gu, G. (2009). Improving the global precipitation record: GPCP Version 2.1. *Geophysical Research Letters*, *36*(17), L17808. https://doi.org/10.1029/2009GL040000

Hung, M.-P., Lin, J.-L., Wang, W., Kim, D., Shinoda, T., &Weaver, S. J. (2013). MJO and Convectively Coupled Equatorial Waves Simulated by CMIP5 Climate Models. *Journal of Climate*, *26*(17), 6185–6214. https://doi.org/10.1175/JCLI-D-12-00541.1

Hurrell, J. W., Holland, M. M., Gent, P. R., Ghan, S., Kay, J. E., Kushner, P. J., et al. (2013). The Community Earth System Model: A Framework for Collaborative Research. *Bulletin of the American Meteorological Society*, *94*(9), 1339–1360. https://doi.org/10.1175/BAMS-D-12-00121.1

Jones, P. D., Lister, D. H., Osborn, T. J., Harpham, C., Salmon, M., &Morice, C. P. (2012). Hemispheric and large-scale land-surface air temperature variations: An extensive revision and an update to 2010. *Journal of Geophysical Research: Atmospheres*, *117*(D5), n/a-n/a. https://doi.org/10.1029/2011JD017139

Kiladis, G. N., Wheeler, M. C., Haertel, P. T., Straub, K. H., &Roundy, P. E. (2009). Convectively coupled equatorial waves. *Reviews of Geophysics*, *47*(2), RG2003. https://doi.org/10.1029/2008RG000266

Kim, D., Sperber, K., Stern, W., Waliser, D., Kang, I.-S., Maloney, E., et al. (2009). Application of MJO Simulation Diagnostics to Climate Models. *Journal of Climate*, *22*(23), 6413–6436. https://doi.org/10.1175/2009JCLI3063.1

Kosaka, Y., &Nakamura, H. (2006). Structure and dynamics of the summertime Pacific–Japan teleconnection pattern. *Quarterly Journal of the Royal Meteorological Society*, *132*(619), 2009–2030. https://doi.org/10.1256/qj.05.204

Kusunoki, S. (2018). Is the global atmospheric model MRI-AGCM3.2 better than the CMIP5 atmospheric models in simulating precipitation over East Asia? *Climate Dynamics*, *51*(11–12), 4489–4510. https://doi.org/10.1007/s00382-016-3335-9

Kusunoki, S., &Arakawa, O. (2015). Are CMIP5 Models Better than CMIP3 Models in Simulating Precipitation over East Asia? *Journal of Climate*, *28*(14), 5601–5621. https://doi.org/10.1175/JCLI-D-14-00585.1

Lau, K.-M., &Chan, P. H. (1988). Intraseasonal and Interannual Variations of Tropical Convection: A Possible Link between the 40–50 Day Oscillation and ENSO? *Journal of the Atmospheric Sciences*, *45*(3), 506–521. https://doi.org/10.1175/1520-0469(1988)045<0506:IAIVOT>2.0.CO;2

Lau, W. K. M., &Waliser, D. E. (Eds.). (2005). *Intraseasonal Variability in the Atmosphere-Ocean Climate System*. Berlin, Heidelberg: Springer Berlin Heidelberg. https://doi.org/10.1007/b138817

Lee, J., Sperber, K. R., Gleckler, P. J., Bonfils, C. J. W., &Taylor, K. E. (2019). *Quantifying the agreement between observed and simulated extratropical modes of interannual variability*. *Climate Dynamics* (Vol. 52). Springer Berlin Heidelberg. https://doi.org/10.1007/s00382-018-4355-4

Lee, W.-L., Liou, K. N., &Wang, C. (2013). Impact of 3-D topography on surface radiation budget over the Tibetan Plateau. *Theoretical and Applied Climatology*, *113*(1–2), 95–103. https://doi.org/10.1007/s00704-012-0767-y

Lee, W.-L., Wang, Y.-C., Shiu, C.-J., Tsai, I., Tu, C.-Y., Lan, Y.-Y., et al. (2020). Taiwan Earth System Model: Description and Evaluation of Mean. *Geoscientific Model Development*. https://doi.org/https://doi.org/10.5194/gmd-2019-377

LinHo, &Wang, B. (2002). The Time–Space Structure of the Asian–Pacific Summer Monsoon: A Fast Annual Cycle View*. *Journal of Climate*, *15*(15), 2001–2019. https://doi.org/10.1175/1520-0442(2002)015<2001:TTSSOT>2.0.CO;2

LinHo, L. H., Huang, X., &Lau, N.-C. (2008). Winter-to-Spring Transition in East Asia: A Planetary-Scale Perspective of the South China Spring Rain Onset. *Journal of Climate*, *21*(13), 3081–3096. https://doi.org/10.1175/2007JCLI1611.1

Liu, X., Easter, R. C., Ghan, S. J., Zaveri, R., Rasch, P., Shi, X., et al. (2012). Toward a minimal representation of aerosols in climate models: description and evaluation in the Community Atmosphere Model CAM5. *Geoscientific Model Development*, *5*(3), 709–739. https://doi.org/10.5194/gmd-5-709-2012

vanLoon, H., &Rogers, J. C. (1978). The Seesaw in Winter Temperatures between Greenland and Northern Europe. Part I: General Description. *Monthly Weather Review*, *106*, 296–310.

Madden, R. A., &Julian, P. R. (1972). Description of Global-Scale Circulation Cells in the Tropics with a 40–50 Day Period. *Journal of the Atmospheric Sciences*, *29*(6), 1109–1123. https://doi.org/10.1175/1520-0469(1972)029<1109:DOGSCC>2.0.CO;2

Meehl, G. A., Senior, C. A., Eyring, V., Flato, G., Lamarque, J.-F., Stouffer, R. J., et al. (2020). Context for interpreting equilibrium climate sensitivity and transient climate response from the CMIP6 Earth system models. *Science Advances*, *6*(26), eaba1981. https://doi.org/10.1126/sciadv.aba1981

Murakami, H., Mizuta, R., &Shindo, E. (2012). Future changes in tropical cyclone activity projected by multi-physics and multi-SST ensemble experiments using the 60-km-mesh MRI-AGCM. *Climate Dynamics*, *39*(9–10), 2569–2584. https://doi.org/10.1007/s00382-011-1223-x

Murakami, H., Wang, Y., Yoshimura, H., Mizuta, R., Sugi, M., Shindo, E., et al. (2012). Future Changes in Tropical Cyclone Activity Projected by the New High-Resolution MRI-AGCM. *Journal of Climate*, *25*(9), 3237–3260. https://doi.org/10.1175/JCLI-D-11-00415.1

Murakami, T., &Matsumoto, J. (1994). Summer Monsoon over the Asian Continent and Western North Pacific. *Journal of the Meteorological Society of Japan. Ser. II*, *72*(5), 719–745. https://doi.org/10.2151/jmsj1965.72.5_719

N. Takayabu, Y. (1994). Large-Scale Cloud Disturbances Associated with Equatorial Waves. *Journal of the Meteorological Society of Japan. Ser. II*, *72*(3), 433–449. https://doi.org/10.2151/jmsj1965.72.3_433

Nitta, T. (1987). Convective Activities in the Tropical Western Pacific and Their Impact on the Northern Hemisphere Summer Circulation. *Journal of the Meteorological Society of Japan. Ser. II*, *65*(3), 373–390. https://doi.org/10.2151/jmsj1965.65.3_373

Potter, G. L., Carriere, L., Hertz, J., Bosilovich, M., Duffy, D., Lee, T., &Williams, D. N. (2018). Enabling Reanalysis Research Using the Collaborative Reanalysis Technical Environment (CREATE). *Bulletin of the American Meteorological Society*, *99*(4), 677–687. https://doi.org/10.1175/BAMS-D-17-0174.1

Rayner, N. A., Parker, D. E., Folland, C. K., Alexander, L. V., Rowell, D. P., Kent, E. C., &Kapland, A. (2003). Global analyses of sea surface temperature, sea ice, and night marine air temperature since the late nineteenth century. *Journal of Geophysical Research*, *108*(D14), 4407. https://doi.org/10.1029/2002JD002670

Rogers, J. C., &vanLoon, H. (1979). The Seesaw in Temperatures between Greenland and Northern Europe. Part II: Some Oceanic and Atmospheric Effects in Middle and High Latitudes. *Monthly Weather Review*, *107*, 509–519.

Rohde, R., Muller, R. A., Jacobsen, R., Muller, E., Perimutter, S., Rosenfeld, A., et al. (2013). A New Estimate of the Average Earth Surface Land Temperature Spanning 1753 to 2011. *Geoinformatics & Geostatistics: An Overview*, *01*(01). https://doi.org/10.4172/2327-4581.1000101

Shiu, C.-J., Wang, Y.-C., Hsu, H.-H., Chen, W.-T., Pan, H.-L., Sun, R., et al. (2020). GTS v1.0: A Macrophysics Scheme for Climate Models Based on a Probability Density Function. *Geoscientific Model Development*. https://doi.org/10.5194/gmd-2020-144

Smith, G. L., Priestley, K. J., Loeb, N. G., Wielicki, B. A., Charlock, T. P., Minnis, P., et al. (2011). Clouds and Earth Radiant Energy System (CERES), a review: Past, present and future. *Advances in Space Research*, *48*(2), 254–263. https://doi.org/10.1016/j.asr.2011.03.009

Stephens, G. L., L'Ecuyer, T., Forbes, R., Gettelmen, A., Golaz, J.-C., Bodas-Salcedo, A., et al. (2010). Dreary state of precipitation in global models. *Journal of Geophysical Research: Atmospheres*, *115*(D24). https://doi.org/10.1029/2010JD014532

Suzuki, S., &Hoskins, B. (2009). The Large-Scale Circulation Change at the End of the Baiu Season in Japan as Seen in ERA40 Data. *Journal of the Meteorological Society of Japan*, *87*(1), 83–99. https://doi.org/10.2151/jmsj.87.83

Taylor, K. (2001). Summarizing multiple aspects of model performance in a single diagram. *J. Geophys. Res*, *106*(D7), 7183–7192. Retrieved from http://www.agu.org/journals/jd/jd0107/2000JD900719/pdf/2000JD900719.pdf

Thompson, D. W. J., &Wallace, J. M. (1998). The Arctic oscillation signature in the wintertime geopotential height and temperature fields. *Geophysical Research Letters*, *25*(9), 1297–1300. https://doi.org/10.1029/98GL00950

Walker, G. T., &Bliss, E. W. (1932). World Weather V. *Memoirs of the Royal Meteorological Society*, *4*, 53–84.

Wallace, J. M., &Gutzler, D. S. (1981). Teleconnections in the Geopotential Height Field during the Northern Hemisphere Winter. *Monthly Weather Review*, *109*(4), 784–812. https://doi.org/10.1175/1520-0493(1981)109<0784:TITGHF>2.0.CO;2

Wang, B., Wu, R., &Fu, X. (2000). Pacific–East Asian Teleconnection: How Does ENSO Affect East Asian Climate? *Journal of Climate*, *13*(9), 1517–1536. https://doi.org/10.1175/1520-0442(2000)013<1517:PEATHD>2.0.CO;2

Wang, Y. C., &Hsu, H. H. (2019). Improving diurnal rainfall phase over the Southern Great Plains in warm seasons by using a convective triggering design. *International Journal of Climatology*, *39*(13), 5181–5190. https://doi.org/10.1002/joc.6117

Wang, Y. C., Pan, H. L., &Hsu, H. H. (2015). Impacts of the triggering function of cumulus parameterization on warm-season diurnal rainfall cycles at the Atmospheric Radiation Measurement Southern Great Plains Site. *Journal of Geophysical Research*, *120*(20), 10,681-10,702. https://doi.org/10.1002/2015JD023337

Wheeler, M., &Kiladis, G. N. (1999). Convectively Coupled Equatorial Waves: Analysis of Clouds and Temperature in the Wavenumber–Frequency Domain. *Journal of the Atmospheric Sciences*, *56*(3), 374–399. https://doi.org/10.1175/1520-0469(1999)056<0374:CCEWAO>2.0.CO;2

Wielicki, B. A., Barkstrom, B. R., Harrison, E. F., Lee, R. B., Louis Smith, G., &Cooper, J. E. (1996). Clouds and the Earth's Radiant Energy System (CERES): An Earth Observing

System Experiment. *Bulletin of the American Meteorological Society*, *77*(5), 853–868. https://doi.org/10.1175/1520-0477(1996)077<0853:CATERE>2.0.CO;2

Wu, C.-H., Kau, W.-S., &Chou, M.-D. (2009). Summer monsoon onset in the subtropical western North Pacific. *Geophysical Research Letters*, *36*(18), L18810. https://doi.org/10.1029/2009GL040168

Wu, C.-H., Hsu, H.-H., &Chou, M.-D. (2014). Effect of the Arakan Mountains in the northwestern Indochina Peninsula on the late May Asian monsoon transition. *Journal of Geophysical Research: Atmospheres*, *119*(18), 10,769-10,779. https://doi.org/10.1002/2014JD022024

Wu, C.-H., Wang, S.-Y. S., &Hsu, H.-H. (2018). Large-scale control of the Arabian Sea monsoon inversion in August. *Climate Dynamics*, *51*(7–8), 2581–2592. https://doi.org/10.1007/s00382-017-4029-7

Zelinka, M. D., Myers, T. A., McCoy, D. T., Po-Chedley, S., Caldwell, P. M., Ceppi, P., et al. (2020). Causes of Higher Climate Sensitivity in CMIP6 Models. *Geophysical Research Letters*, *47*(1). https://doi.org/10.1029/2019GL085782

Zhang, C. (2005). Madden-Julian Oscillation. *Reviews of Geophysics*, *43*(2), RG2003. https://doi.org/10.1029/2004RG000158

Journal of Advances in Modeling Earth Systems

Supporting Information for

Performance of the Taiwan Earth System Model in Simulating Climate Variability Compared with Observations and CMIP6 Model Simulations

Yi-Chi Wang[1], Huang-Hsiung Hsu[1], Chao-An Chen[1], Wan-Ling Tseng[1], Pei-Chun Hsu[1], Yu-Luen Chen[1], Chien-Wei Lin[1], Li-Chiang Jiang[1], Yu-Chi Lee[1], Hsin-Chien Liang[1], and Lex Chang[1]

[1]Research Center for Environmental Changes, Academia Sinica, Taipei, Taiwan

Contents of this file

Text S1 to S2
Figures S1
Tables S1 to S2

Introduction

The supporting texts describe the metrics used in the analyses of intraseasonal variability in Section 5. Text S1 provides the description of metrics shown in the summary diagram of intraseasonal variability (Figure 6). Text S2 provides the description of metrics shown in the summary diagram of convective coupled equatorial wave (Figure 7).

The supporting figure shows the four major monsoon regions discussed in Section 4 and analyzed in Figure 4 and 5.

The supporting tables provide detailed information for model data and observations used in this study. Table S1 shows the complete list of all models used for each analysis in this study. Information of each model can be found in the CMIP6 archive hosted by Lawrence Livermore National Laboratory, Department of Energy (http://esgf-node.llnl.gov/search/cmip6/). Table S2 provides details of the observation dataset and variables used to evaluate model performance.

Text S1. Description of metrics used in analysis of intraseasonal variability (Figure 6).

The summary diagram in Figure 6d is based on the metrics defined in previous studies for intraseasonal variation (CLIVAR Madden-Julian Oscillation working group, 2009; Hendon & Wheeler, 2008; Kim et al., 2009; Neena et al., 2017). Two seasons are defined: boreal winter (November to April) and boreal summer (May to October). The broadbands 20–100-day intraseasonal variance for boreal winter and 20–90-day intraseasonal variance for summer are illustrated. The left Y-axis represents the skill scores, as described in Section 2. The right Y-axis is defined as the ratio of the absolute value between the models and observations and multiplied by -1 to keep the better models on top. Therefore, in both indices, a higher value represents better simulation ability. The winter parameters are W1–W3. W1 is the eastward/westward (E/W) ratio of 850-hPa zonal wind, calculated as the sum of eastward propagating power divided by the westward propagating counterpart within wavenumber 1–2 and a period of 30–80 days, as shown in Fig. 6a (Kim et al., 2009). W2 is the sum of RMM1 and RMM2 variance with reference to Hendon and Wheeler (2008) but only in the winter season. W3 is the eastward propagation tendency of precipitation correlated with the Indian Ocean (10°S–5°N, 75°E–100°E) precipitation base in Fig. 6b. Regressed anomalies are averaged over 10°S–10°N. The computational domain of the skill score is averaged over 0°–150°W (210°) and lag day −20 to 20. Likewise, the summer parameters are S1–S3, which are similar to W3 but for the summer season. S1 is the eastward propagation tendency of the precipitation correlated with the Indian Ocean (EEIO; 5°S-5°N, 75°E-85°E) precipitation base according to Neena et al. (2017). Regressed anomalies are averaged over 10°S–10°N. The computational domain of the skill score is averaged over 30°E–150°W and lag day −20 to 20. S2 is the northward propagation tendency correlated with the near equatorial region (NEO; 5°N–10°N, 85°E–90°E), similar to S1, with regressed anomalies averaged over 80°E–100°E. The computational domain of the skill score is averaged over 10°S–25°N and lag day −20 to 20. S3 is the westward propagation tendency correlated with the Bay of Bengal region (BOB; 10°N–15°N, 85°E–90°E), similar to S1, with regressed anomalies averaged over 10°N–15°N. The computational domain of the skill score is averaged over 80°E–150°E and lag day −20 to 20.

Text S2. Description of metrics used in analysis of intraseasonal variability (Figure 6).

The summary diagram in Figure 7c is based on analyses of previous studies (CLIVAR Madden-Julian Oscillation working group, 2009; Dias & Kiladis, 2014; Hendon & Wheeler, 2008; Kim et al., 2009; Neena et al., 2017; Wheeler & Kiladis, 1999). Four seasons are defined: March–May (MAM), June–August (JJA), September–November (SON), and December–February (DJF). The Y-axis represents the skill score, which is described in Section 2. The annual skill scores of eastward (01) and westward (02) propagation are based on spectra in Fig. 7a, and those based on spatial patterns of EK and ER waves based on seasonal precipitation are shown with (03) to (10). The skill score is calculated at 30˚S–30˚N along with the global belt.

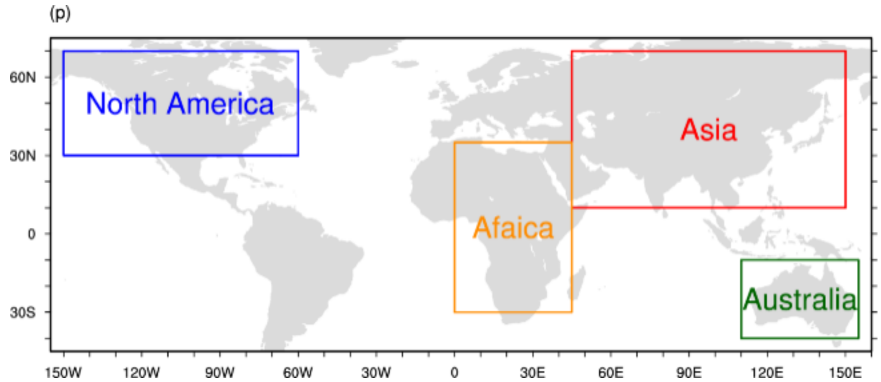

Figure S1. Four major monsoon regions analyzed in analysis for seasonal evolution (Figures 4 and 5).

	Historical TAS	Mean state	ENSO	Monsoon	Extreme rainfall	Synoptic eddies	intraseasonal	Teleconnection/interannual/interdecadal	Diurnal rainfall
Data frequency	mon	mon	mon	mon	daily	daily	daily	mon	3-hrly
Number of models used	46	37	29	37	28	10	14	37	12
ACCESS-CM2	v	v		v	v			v	
ACCESS-ESM1-5	v	v		v	v			v	
AWI-ESM-1-1-LR	v	v		v				v	
AWI-CM-1-1-MR									v
BCC-CSM2-MR	v	v	v	v	v	v	v	v	v
BCC-ESM1	v	v	v	v	v	v	v	v	
CAMS-CSM1-0	v	v	v	v				v	
CanESM5	v	v	v	v	v	v	v	v	
CESM2-FV2	v	v	v	v	v			v	
CESM2	v	v	v	v	v	v	v	v	v
CESM2-WACCM-FV2	v	v	v	v	v			v	
CESM2-WACCM	v	v	v	v	v	v	v	v	
CIESM	v	v	v	v				v	
CMCC-CM2-SR5	v	v		v				v	
CNRM-CM6-1	v				v		v		
E3SM-1-0	v								
E3SM-1-1	v								
E3SM-1-1-ECA	v	v	v	v				v	

EC-EARTH3	v	v		v	v		v	v	v
EC-EARTH3-Veg	v	v	v	v	v	v	v	v	
EC-EARTH3-Veg-LR	v	v		v				v	
FGOALS-g3	v	v	v	v				v	
FIO-ESM-2-0	v								
GFDL CM4	v	v	v	v	v	v	v	v	v
GFDL-ESM4	v	v	v	v	v			v	
GISS-E2-1-G	v	v	v	v	v	v	v	v	v
GISS-E2-1-H	v	v	v	v				v	
HadGEM3-GC31-LL	v								
INM-CM4-8	v	v	v	v	v			v	
INM-CM5-0	v	v	v	v	v			v	
IPSL-CM6A-LR	v	v	v	v	v	v	v	v	v
KACE-1-0-G	v	v		v				v	
MCM-UA-1-0	v								
MIROC6	v	v	v	v	v			v	v
MIROC-ES2L	v								
MRI-ESM2-0	v	v	v	v	v	v	v	v	v
MPI-ESM1-2-HAM	v	v	V	v	v			v	
MPI-ESM1-2-HR	v	v		v	v			v	

MPI-ESM1-2-LR	v	v	v	v	V			v	
NESM3	v	v	v	v				v	v
NorCPM1	v	v	v	v	v			v	
NorESM2-LM	v	v	v	v	v			v	
NorESM2-MM	v	v	v	v	v			v	
SAM0-UNICON	v	v	v	v	v	v	v	v	v
TaiESM	v	v	v	v	v	v	v	v	v
UKESM1-0-LL	v								

Table S1. List of CMIP6 models used in the analysis.

Data name	Period	Variables
Mean state		
GPCP	1980–2014	pr
	GPCP Version 2.3 Combined Precipitation Dataset (GPCP-SG_L3_v2.3; Final; Adler et al., 2003; Huffman et al., 1997)	
MRE2 ensemble	1980–2014	ua, va, ta, zg, tas, ts
	CREATE-MRE (Collaborative REAnalysis Technical Environment - Multiple Reanalysis Ensemble; Bosilovich et al., 2009) CREATE-IP data access: https://esgf.nccs.nasa.gov/projects/create-ip.	
CERES	2001–2013	rlut, rsut, rlutcs, rsutcs
	CERES EBAF: Clouds and Earth's Radiant Energy Systems (CERES) Energy Balanced and Filled (EBAF; Loeb et al., 2018; Wielicki et al., 1996)	
ENSO analysis		
MRE2 ensemble	1980–2014	Ts, slp, u1000, v1000
Monsoon analysis		
GPCP	1980–2014	pr
MRE2 ensemble	1980–2014	ua, va, zg, psl
Extreme rainfall		
GPCP	1998–2014	pr
	1-degree grid data of the Global Precipitation Climatology Project (GPCP), version 1.2 (Huffman et al., 2001)	
Synoptic eddies		
MRE2 ensemble	1980–2014	ua, va, ta
MJO		
GPCP	1998–2014	pr
NOAA OLR		olr
	NOAA Interpolated Outgoing Longwave Radiation (OLR; Liebmann & Smith, 1996)	
ERA-Interim	1980–2014	u850
	ECMWF Re-Analysis Interim (ERA-Interim; Dee et al., 2011)	
Teleconnection/interannual/interdecadal oscillation		
MRE2 ensemble	1980–2014	ua, va, zg, psl
HadISST 1.1	1915–2014	SST
	HadISST 1.1 monthly average sea surface temperature (Rayner et al., 2003)	
Historical warming		
BEST	1950–2014	2-m temperature

	Berkeley Earth Surface Temperatures (Rohde et al., 2013)	
HadCRU	1950–2014	2-m temperature
	Hadley Centre-Climate Research Unit Temperature Anomalies (Jones et al., 2012)	

Table S2. List of observations used in the analysis.

References

Adler, R. F., Huffman, G. J., Chang, A., Ferraro, R., Xie, P.-P., Janowiak, J., et al. (2003). The Version-2 Global Precipitation Climatology Project (GPCP) Monthly Precipitation Analysis (1979–Present). *Journal of Hydrometeorology*, *4*(6), 1147–1167. https://doi.org/10.1175/1525-7541(2003)004<1147:TVGPCP>2.0.CO;2

Bosilovich, M. G., Mocko, D., Roads, J. O., &Ruane, A. (2009). A Multimodel Analysis for the Coordinated Enhanced Observing Period (CEOP). *Journal of Hydrometeorology*, *10*(4), 912–934. https://doi.org/10.1175/2009JHM1090.1

CLIVAR Madden-Julian Oscillation working group. (2009). MJO Simulation Diagnostics. *Journal of Climate*, *22*(11), 3006–3030. https://doi.org/10.1175/2008JCLI2731.1

Dee, D. P., Uppala, S. M., Simmons, A. J., Berrisford, P., Poli, P., Kobayashi, S., et al. (2011). The ERA-Interim reanalysis: configuration and performance of the data assimilation system. *Quarterly Journal of the Royal Meteorological Society*, *137*(656), 553–597. https://doi.org/10.1002/qj.828

Dias, J., &Kiladis, G. N. (2014). Influence of the basic state zonal flow on convectively coupled equatorial waves. *Geophysical Research Letters*, *41*(19), 6904–6913. https://doi.org/10.1002/2014GL061476

Hendon, H. H., &Wheeler, M. C. (2008). Some Space–Time Spectral Analyses of Tropical Convection and Planetary-Scale Waves. *Journal of the Atmospheric Sciences*, *65*(9), 2936–2948. https://doi.org/10.1175/2008JAS2675.1

Huffman, G. J., Adler, R. F., Arkin, P., Chang, A., Ferraro, R., Gruber, A., et al. (1997). The Global Precipitation Climatology Project (GPCP) Combined Precipitation Dataset. *Bulletin of the American Meteorological Society*, *78*(1), 5–20. https://doi.org/10.1175/1520-0477(1997)078<0005:TGPCPG>2.0.CO;2

Huffman, G. J., Adler, R. F., Morrissey, M. M., Bolvin, D. T., Curtis, S., Joyce, R., et al. (2001). Global Precipitation at One-Degree Daily Resolution from Multisatellite Observations. *Journal of Hydrometeorology*, *2*(1), 36–50. https://doi.org/10.1175/1525-7541(2001)002<0036:GPAODD>2.0.CO;2

Jones, P. D., Lister, D. H., Osborn, T. J., Harpham, C., Salmon, M., &Morice, C. P. (2012). Hemispheric and large-scale land-surface air temperature variations: An extensive revision and an update to 2010. *Journal of Geophysical Research: Atmospheres*, *117*(D5), n/a-n/a. https://doi.org/10.1029/2011JD017139

Kim, D., Sperber, K., Stern, W., Waliser, D., Kang, I.-S., Maloney, E., et al. (2009). Application of MJO Simulation Diagnostics to Climate Models. *Journal of Climate*, *22*(23), 6413–6436. https://doi.org/10.1175/2009JCLI3063.1

Liebmann, B., &Smith, C. A. (1996). Description of a Complete (Interpolated) Outgoing Longwave Radiation Dataset. *Bulletin of the American Meteorological Society*, *77*(6), 1275–1277. Retrieved from http://www.jstor.org/stable/26233278

Loeb, N. G., Su, W., Doelling, D. R., Wong, T., Minnis, P., Thomas, S., &Miller, W. F. (2018). Earth's Top-of-Atmosphere Radiation Budget. In *Comprehensive Remote Sensing* (pp. 67–84). Elsevier. https://doi.org/10.1016/B978-0-12-409548-9.10367-7

Neena, J. M., Waliser, D., &Jiang, X. (2017). Model performance metrics and process diagnostics for boreal summer intraseasonal variability. *Climate Dynamics*, *48*(5–6), 1661–1683. https://doi.org/10.1007/s00382-016-3166-8

Rayner, N. A., Parker, D. E., Folland, C. K., Alexander, L. V., Rowell, D. P., Kent, E. C., &Kapland, A. (2003). Global analyses of sea surface temperature, sea ice, and night marine air temperature since the late nineteenth century. *Journal of Geophysical Research*, *108*(D14), 4407. https://doi.org/10.1029/2002JD002670

Rohde, R., Muller, R. A., Jacobsen, R., Muller, E., Perimutter, S., Rosenfeld, A., et al. (2013). A New Estimate of the Average Earth Surface Land Temperature Spanning 1753 to 2011. *Geoinformatics & Geostatistics: An Overview*, *01*(01). https://doi.org/10.4172/2327-4581.1000101

Wheeler, M., &Kiladis, G. N. (1999). Convectively Coupled Equatorial Waves: Analysis of Clouds and Temperature in the Wavenumber–Frequency Domain. *Journal of the Atmospheric Sciences*, *56*(3), 374–399. https://doi.org/10.1175/1520-0469(1999)056<0374:CCEWAO>2.0.CO;2

Wielicki, B. A., Barkstrom, B. R., Harrison, E. F., Lee, R. B., Louis Smith, G., &Cooper, J. E. (1996). Clouds and the Earth's Radiant Energy System (CERES): An Earth Observing System Experiment. *Bulletin of the American Meteorological Society*, *77*(5), 853–868. https://doi.org/10.1175/1520-0477(1996)077<0853:CATERE>2.0.CO;2